Seasonal variations of sea ice and ocean circulation in the Bering Sea: A model-data fusion study

Jia Wang,[1] Haoguo Hu,[2] Kohei Mizobata,[3] and Sei-ichi Saitoh[4]

Received 8 January 2008; revised 30 May 2008; accepted 2 September 2008; published 13 February 2009.

[1] A 9-km coupled ice-ocean model (CIOM) was implemented in the entire Bering Sea to investigate seasonal cycles of sea ice and ocean circulation under atmospheric forcing. Sea ice cover with a maximum of 0.6×10^6 km^2 in February to late March was reasonably reproduced by the Bering-CIOM and validated by Special Sensor Microwave/Imager (SSM/I) measurements. The model also captures some important spatial variability and downscaling processes such as polynyas and ridging, which the SSM/I measurements cannot reproduce because of their coarse (25 km) resolution. There are two distinct surface ocean circulation patterns in winter and summer on the Bering shelves because of the dominant winds, which are northeasterly in winter and southwesterly in summer. Summer low-temperature, high-salinity water mass (<3°C) on the Bering shelf is formed locally during winter because of strong vertical convection caused by salt injection when ice forms, wind, and wind-wave mixing on the shelf. The northward volume transport across the 62.5°N line, with an annual mean of 0.8 ± 0.33 Sv (1 Sv = 10^6 m^3 s^{-1}) that is consistent with the measurements in the Bering Strait, has barotropic structure, which transports heat flux (with an annual mean of 7.74 TW; 1 TW = 10^{12} W) northward. The Anadyr Current advects warmer, saltier water northward during summer; nevertheless, it reverses its direction to southward during winter because of predominant northeasterly and northerly wind forcing. Therefore, the Anadyr Current advects cold, salty water southward. The volume transport on the broad midshelf is northward year round, advecting heat (3.3 ± 2.4 TW) and freshwater ($-8 \pm 10 \times 10^4$ practical salinity unit (psu) m^3 s^{-1}) northward. One important finding is that the Anadyr Current and the midshelf current are out of phase in volume and heat transports. The Alaskan Coastal Current also transports heat and freshwater northward on an annual basis. The Bering-CIOM also captures the winter dense water formation along the Siberian coast, which is promoted by the downwelling favorable northeasterly wind, and the summer upwelling due to the basin-scale upwelling favorable southwesterly wind, which brings up the cold, salty, and nutrient-rich water from the subsurface to the surface within a narrow strip along the west coast. This upwelling found in the model was also confirmed by satellite measurements in this study.

Citation: Wang, J., H. Hu, K. Mizobata, and S. Saitoh (2009), Seasonal variations of sea ice and ocean circulation in the Bering Sea: A model-data fusion study, *J. Geophys. Res.*, *114*, C02011, doi:10.1029/2008JC004727.

1. Introduction

[2] The northern North Pacific Ocean, including the Bering Sea and the Gulf of Alaska, is among the most productive marine ecosystems in the world, as evidenced by large populations of marine and freshwater salmon, fish, birds, and mammals. This productivity is critical not only to the U.S. economy, since fish and shellfish from these regions constitute more than 10% of the world and about 52% of the U.S. seafood harvest, but also to the economy of surrounding countries.

[3] The Bering Sea (Figure 1) is a complex semienclosed basin with shallow shelves, shelf breaks, and deep basins. The ocean circulation pattern is complicated (Figure 1). The Alaskan Stream (AS) mainly flows along the Aleutian Peninsula and provides some of its water via Aleutian passes to the Bering Slope Current (BSC) and the Alaskan Coastal Water (ACW) or Alaskan Coastal Current (ACC), and also to the Aleutian North Slope Current (ANSC [*Stabeno et al.*, 1999]). The BSC splits into two coastal currents: the Anadyr Current (AC), which flows along the west coast into the Chukchi Sea through the western side of Bering Strait, and the southwestern coastal current, which

[1]Great Lakes Environmental Research Laboratory, NOAA, Ann Arbor, Michigan, USA.
[2]Cooperative Institute for Limnology and Ecosystems Research, School of Natural Resources and Environment, University of Michigan, Ann Arbor, Michigan, USA.
[3]Department of Ocean Sciences, Tokyo University of Marine Science and Technology, Tokyo, Japan.
[4]Graduate School of Fisheries Sciences, Hokkaido University, Hakodate, Japan.

0148-0227/09/2008JC004727

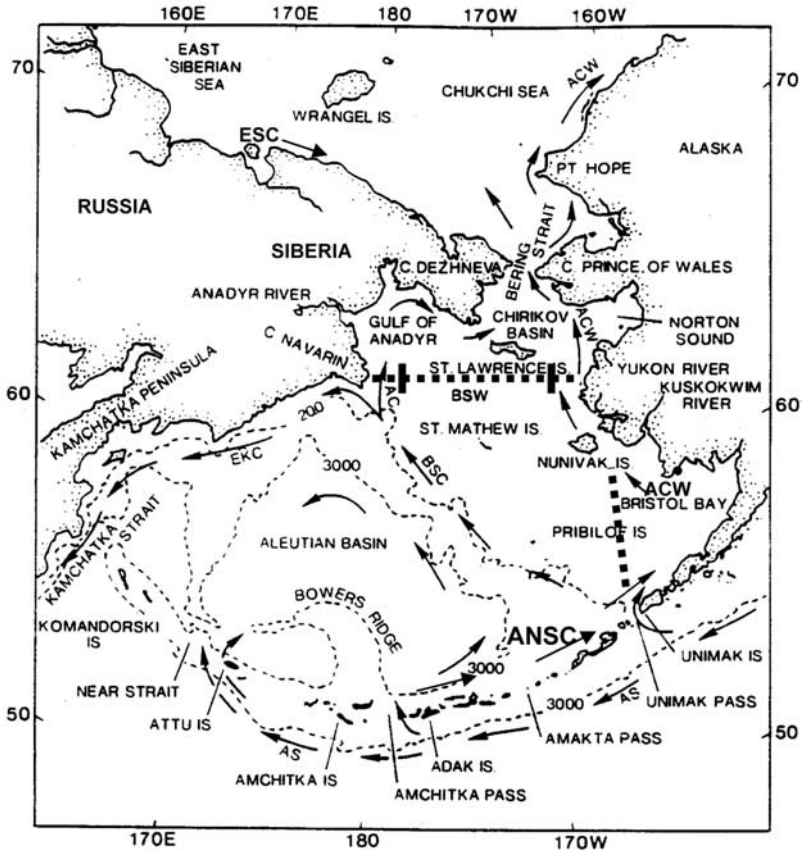

Figure 1. Topography and bathymetry of the Bering Sea and the schematic circulation systems (by arrows). The model domain is from 49.5 to 66.5°N and 160°E–160°W. The 166°W line and 62.5°N line are dashed. Along the 62.5°N line, three subsections are divided by the vertical lines: (1) the Anadyr Current section (at west), (2) midshelf section (middle), and (3) the Alaskan Coastal Current section (at east). Water depths are in meters.

forms the East Kamchatka Current (EKC). Numerous possible mesoscale eddy generation sites exist within the AS and BSC, due to the interaction between baroclinic instability and the continental slope [*Wang and Ikeda*, 1997; *Mizobata et al.*, 2002, 2006, 2008]. The basic schematic surface circulation pattern is fairly well known (Figure 1), on the basis of available observational evidence [*Kinder and Coachman*, 1978; *Stabeno and Reed*, 1994]. The interaction or exchange between shelves and deep basins is a typical phenomenon that significantly influences primary and secondary productivity [*Mizobata et al.*, 2002; *Mizobata and Saitoh*, 2004].

[4] Ecosystem dynamics related to physical forcing have been summarized by the Inner Shelf Transfer and cycling in the Bering-Chukchi Seas (ISHTAR) Program [*Coachman and Handell*, 1993]. A detailed review of the Bering Sea "Green Belt" has also been conducted by *Springer et al.* [1996]. The Bering Sea shelf edge processes and ecosystem productivity are the key focus in the area. The high productivity near the shelf break (i.e., along the AS and BSC) is qualitatively described. There are some hypotheses linking high productivity to climate change, shelf-basin exchanges, upwelling, nutrient pumping due to internal tides, etc. However, these hypotheses need to be tested by both observations and sophisticated ice-ocean models in realistic settings.

[5] In the past several decades, the Pacific Decadal Oscillation (PDO) [*Mantua et al.*, 1997], and Arctic Oscillation (AO) [*Thompson and Wallace*, 1998] have significantly impacted climate change not only in the Arctic region [*Wang and Ikeda*, 2000; *Wang et al.*, 2005b], but also in the Bering Sea [*Wang and Ikeda*, 2001] in a competitive manner, as evidenced by the increase in surface air temperature (SAT), sea surface temperature (SST) [*Minobe*, 1999; *Luchin et al.*, 1999], and decline in sea ice cover [*Hunt et al.*, 2002; *Overland and Stabeno*, 2004]. This dramatic climate change may be related to spectacular declines in some marine mammal and bird populations. The Bering Sea is the world's third largest semienclosed sea, and has water exchange with both the Arctic Ocean (via the Bering Strait) and the North Pacific. An understanding of both the ice-ocean circulation system and the biocomplexity in this topographically and geometrically complex region is important when (1) assessing the role of water exchange between the Bering and Chukchi Seas, (2) improving our knowledge of the effects of physical variables on primary and secondary productivity, and (3) elucidating the relationship between both factors.

[6] Sea ice in the Bering Sea is first-year ice, with ice thickness being typically 0.5–2.0 m [*Niebauer*, 1980]. Seasonal variation is the dominant phenomenon [*Tateyama*

and Enomoto, 2001; *Wang and Ikeda*, 2001], though interannual and decadal variability is significant because of the teleconnection of the Aleutian Low to the tropical Southern Oscillation (SO) [*Wallace and Gutzler*, 1981], the so-called PNA (Pacific–North America) pattern. The North Pacific Oscillation (NPO) [*Minobe*, 1999], which may be coupled to the AO [*Thompson and Wallace*, 1998; *Wang and Ikeda*, 2000, 2001], is also an important predictor in the region. Thus, the synoptic cyclone frequency, pathway, and intensity, and the resulting precipitation (that is equivalent to river/glacier freshwater runoff of the following year) all depend on these climate patterns.

[7] In the Bering Sea, sea ice cover is an important predictor of regional climate [*Niebauer*, 1980; *Wang and Ikeda*, 2001]. Sea ice extent also determines ocean circulation patterns and thermal structure because (1) wind stress drag is different in magnitude over water surface than over ice surface [*Pease et al.*, 1983]; (2) the albedo over ice versus water differs, and thus, prediction of the sea ice extent (i.e., edge) is crucial to predicting the ocean mixed layer and ocean circulation, and thus, to predicting primary and secondary productivity [*Springer et al.*, 1996]; and (3) spring ice melt freshwater increases stratification in the upper layer, which may enhance phytoplankton blooms. In addition, climate change, through its effect on the timing of ice melting, would determine the timing of phytoplankton and zooplankton blooms. As a result, sea ice conditions and the ecosystem in the Bering Sea will be driven mainly by atmospheric forcing, from tidal, synoptic, and seasonal, to interannual and decadal time scales.

[8] Extensive oceanographic and fisheries observations have been conducted in the past several decades. Hydrographic measurements include typical CTD stations and transects, current meter moorings [*Cokelet and Stabeno*, 1997; *Onishi and Ohtani*, 1999], towed/mounted ADCP (Acoustic Doppler Current Profiler) transects [*Cokelet et al.*, 1996], and satellite tracked buoys [*Stabeno and Reed*, 1994]. The major dynamic features in the Bering Sea are very rich: tide/wind-dominated shelves, deep basin circulation and eddies [*Cokelet et al.*, 1996], frontal instability between the deep basin and the Bering shelf [*Kinder and Coachman*, 1978; *Belkin and Cornillon*, 2005], and mesoscale eddies pinched off from the BSC [*Kinder et al.*, 1980; *Mizobata et al.*, 2002, 2006]. However, the regional observational studies mentioned above lack a systematic, quantitative understanding of the connection between those physical processes and primary productivity. Thus, a coupled ice-ocean model is essential for better understanding of the ocean general circulation from tidal to synoptic to climate time scales in the Bering Sea.

[9] An ocean-only model for the Bering-Chukchi shelves was developed during the ISHTAR Program by *Nihoul et al.* [1993]. Though the ISHTAR model includes both tidal and wind forcing, the deep basin was excluded (i.e., the AS, BSC, AC, and KC were excluded). Thus the heat and freshwater fluxes, as well as the AS, were neglected. In consequence, there is yet much to understand concerning this ocean system. Because of using an ocean-only model, the simulation was conducted only in the ice-free seasons. There is no seasonal cycle simulation available for a realistic setting for biological cycling.

[10] A regional eddy-resolving ocean-only model, which includes both tidal and subtidal dynamics, was implemented at 4 km resolution to simulate circulation on the southeastern Bering Sea shelf and basin [*Hermann et al.*, 2002]. This model resolved the dominant observed mean currents, eddies, and meanders in the region. Circulation, temperature, and salinity fields for 1995 and 1997 were hindcast, using daily wind and buoyancy flux estimates, and tidal forcing derived from a global model. These hindcast results compared favorably with CTD (conductivity-temperature-depth) data sections, moored current meters, and drogued drifters. However, this ocean–only model does not cover the entire Bering Sea and no seasonal cycles were simulated because there was no ice model. Furthermore, the simulated upper mixed layer depth is of 10 m because no wave mixing was included, which is smaller than the observed value of 20 m.

[11] *Pritchard et al.* [1990] first applied a coupled ice-ocean model to simulate the Bering Sea ice edge using adaptive grids for the ice model. The model resolution is about 50 km. The simulated ice edge variations compared reasonably with the observations. However, no further information such as sea ice thickness, seasonal cycle, and ocean transport, were given.

[12] *Clement et al.* [2005] use a ~9 km pan-Arctic coupled ice-ocean model to investigate the Bering Sea ocean circulation and water exchange via the Bering Strait. Interannual variability of sea ice cover, ocean eddy kinetic energy, and transport were examined. This modeling study provides much information in this area. Nevertheless, the study focuses mainly on ocean transports, and less on sea ice spatial variability, sea ice area, and thickness. Because the model does not include tides and wind-wave mixing, the simulated summer upper surface mixed layer is less than 10 m, which is very shallow compared to observations at ~20 m [*Kinder and Schumacher*, 1981; *Overland et al.*, 1999].

[13] Therefore, we intend to investigate the Bering Sea ocean circulation and sea ice dynamic and thermodynamic features as a whole using the coupled ice-ocean model (CIOM [*Wang et al.*, 2005a]). This model will include parameterized wind-wave mixing to better simulate ocean upper mixed layer depth.

[14] The next section will briefly introduce the CIOM. Section 3 emphasizes model simulations of sea ice in comparison with measurements, both in situ and satellites. Conclusions and discussion are given in section 4.

2. Description of the Bering Sea CIOM and Atmospheric Forcing

[15] The detailed description of development of the CIOM should refer to *Yao et al.* [2000] and *Wang et al.* [2002], which was applied to the pan-Arctic Ocean [*Wang et al.*, 2004a, 2005a; *Wu et al.*, 2004] and Beaufort Sea [*Wang et al.*, 2003a]. The ocean model used is the Princeton Ocean Model (POM) [*Blumberg and Mellor*, 1987; *Mellor*, 2004], and the ice model used is a full thermodynamic and dynamics model [*Hibler*, 1979, 1980] that prognostically simulates sea ice thickness, sea ice concentration (SIC), ice edge, ice velocity, and heat and salt flux through sea ice into the ocean. The model is being applied to the northern China

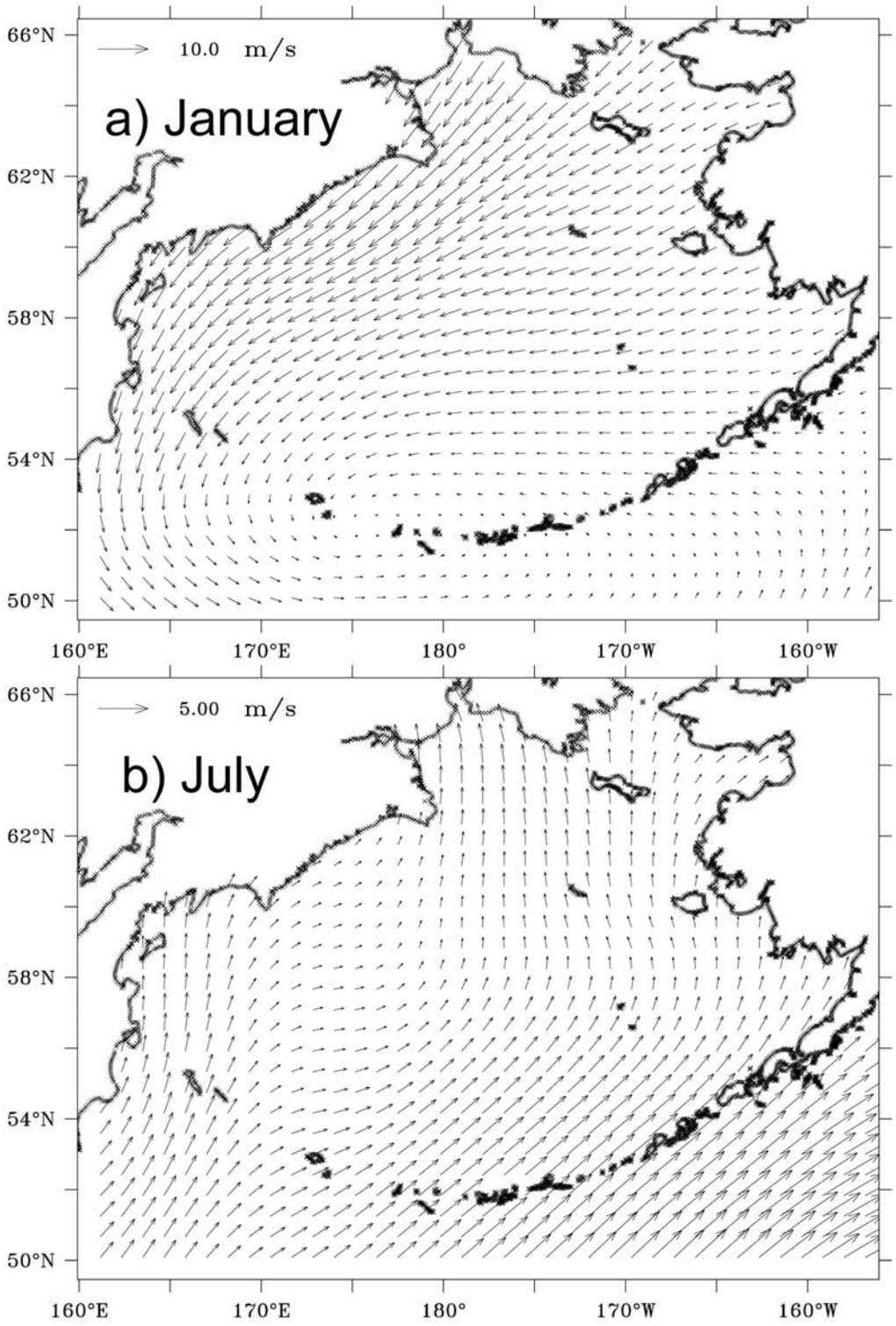

Figure 2. (a) Winter (January) and (b) summer (July) wind fields. Note that the wind speed scaling is different.

seas (Q. Liu, personal communication, 2006) and the Great Lakes.

[16] The Bering-CIOM was configured in horizontal spherical grids with 1/6° longitudes (∼7.4 km in Bering Strait and ∼10 km near the Aleutian Islands) and 1/12° latitudes (∼9.2 km) covering the whole Bering Sea. There are 24 sigma levels in the vertical (at σ = 0, −0.008, −0.016, −0.031, −0.063, −0.125, −0.188, −0.250, −0.313, −0.375, −0.438, −0.500, −0.563, −0.625, −0.688, −0.750, −0.813, −0.875, −0.938, −0.969, −0.984, −0.992, −0.996, −1.). The vertical resolution is higher near the surface and the bottom for a better repre-

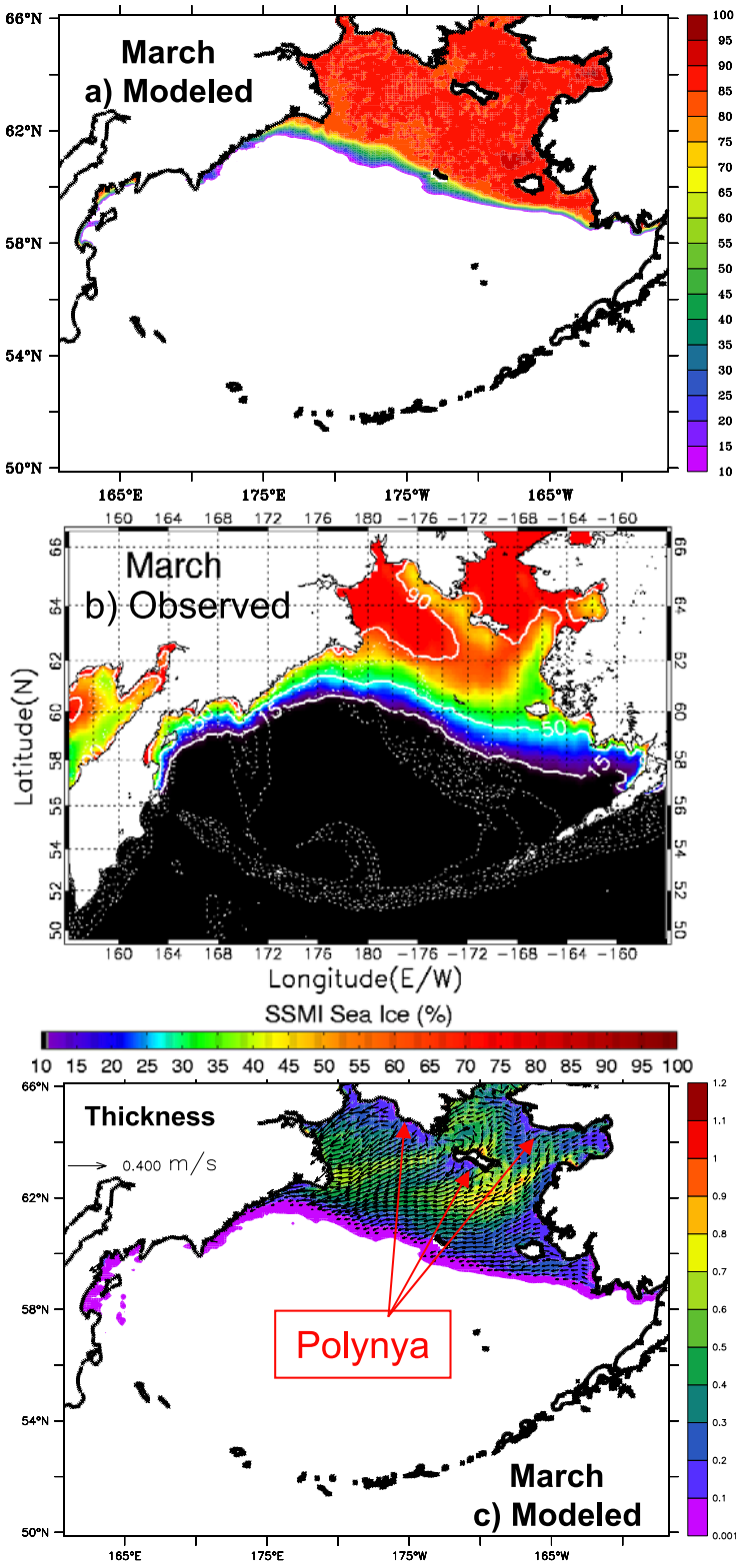

Figure 3. The (a) Bering-CIOM simulated and (b) SSM/I measured sea ice concentration (SIC) and (c) simulated sea ice thickness superimposed by sea ice velocity in March.

sentation of the surface and bottom boundary layers. A parameterization of wind-wave mixing was introduced following *Hu et al.* [2004]. The open boundaries (velocity, T, and S) are embedded by a global climate (atmosphere-ice-ocean-land) model with a resolution of 1/6 × 1/4° (about 25 km [*Watanabe et al.*, 2006]) with volume transport conservation principle and radiation property [*Wang et al.*, 2001].

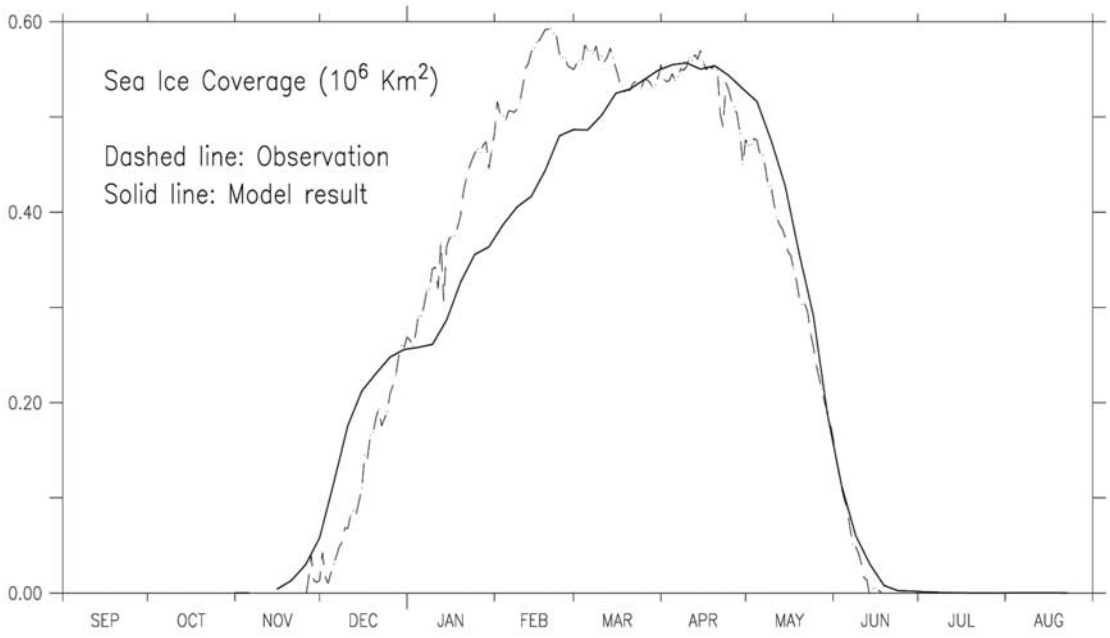

Figure 4. Comparison between the Bering-CIOM simulated seasonal cycle of sea ice area (solid line) and the SSM/I daily climatology (dashed line) averaged from 1996 to 2006.

[17] The ice model has full thermodynamics with 1-layer ice and 1-layer snow and full dynamics with viscous-plastic rheology [*Hibler*, 1979, 1980; *Wang et al.*, 1994]. A multiple thickness category ice model [*Thorndike et al.*, 1975; *Hibler*, 1980; *Yao et al.*, 2000] was used, fully coupled to the ocean model [*Mellor and Kantha*, 1989]. A parameteriztation for the lateral melting of sea ice [*Ohshima and Nihashi*, 2005] was implemented. The prognostic and diagnostic variables include ice velocity, compactness (concentration), ice edge, thickness, etc. In this study, eight ice categories (0, 0.1, 0.2, 0.5, 1.0, 1.5, 2.5, 4 m) are used, each having a percentage in a grid point. Thus, the ice thickness equation for each category is calculated. Then, the summation of each category thickness is the total thickness at each grid. Thus, sea ice concentration and thickness at each grid are calculated from the sum of the eight ice categories.

[18] The bathymetry is obtained from the 5-min resolution ETOPO05 data; however the depths of Aleutian Islands and passes were modified according to NOAA ocean charts [*Office of Coast Survey*, 2004]. Smoothing of topography was conducted with the steep slopes. Subtracting the area-averaged climatological density field before calculating pressure gradient terms was applied to substantially reduce errors to be less than 10% of the mean flow and other numerical errors [*Mellor et al.*, 1994, *Ezer and Mellor*, 1997]. The above procedure is widely used in previous applications of σ coordinate models. The maximum bottom slope allowed between two adjacent grid points is $\Delta H/H < 0.2$. Maximum and minimum depths were set to 3000 m and 10 m, respectively. Upwind advection boundary conditions allow the advection of the monthly mean temperature and salinity into the model domain under inflow conditions. At the open boundaries, vertically averaged inflow/outflow was prescribed using a global model [*Watanabe et al.*, 2006] with adjustment according to observed transport values following *Wang and Mooers* [1998]. For the baroclinic velocities, Sommerfeld type radiation [*Mellor*, 2004] conditions were used. A seasonal cycle was prescribed in such a way that the net annual mean northward transport is 0.8 Sv in the Bering Strait [*Coachman et al.*, 1975; *Coachman and Aagaard*, 1981, 1988; *Roach et al.*, 1995; *Woodgate and Aagaard*, 2005] with the summer transport being ~1.3 Sv, and winter transport being ~0.4 Sv.

[19] The ocean model has split modes. The 2-D external mode uses a time step of 20 s, and the 3-D internal mode uses a time step of 600 s. The sea ice model uses the internal time step, 600 s. The model was spun up using June climatological temperature and salinity from *Steele et al.* [2001] and motionless ocean for the first 6 years under National Centers for Environmental Prediction (NCEP) reanalysis monthly thermodynamic forcing [*Ladd and Bond*, 2002], which were derived from the period of 1958–1997, and monthly wind stress (Figure 2) averaged from NCEP daily winds for period 1996 to 2006. At the surface, salinity, with freshwater flux forcing from precipitation minus evaporation ($P - E$), is restored to the observed monthly salinity fields for prescribing freshwater runoff using the flux correction method of *Wang et al.* [1994, 2001]:

$$K_H \frac{\partial S}{\partial z} = Q_S + C(S_{Obs} - S), \qquad K_H \frac{\partial T}{\partial z} = \frac{Q_H}{\rho C_P},$$

for salt and heat fluxes, where C is the restoring time constant (5.79×10^{-6} ms^{-1}) at a time scale of 30 days. At this rate, the modeled surface salinity (S) is adjusted (or restored) to the respective observed monthly values. Q_S (in units of ms^{-1}) is the E-P or salt flux including freshwater runoff. Q_H (in units of W m^{-2}) is the net surface heat flux calculated from the conventional ice-ocean budget [*Wang et al.*, 2005a].

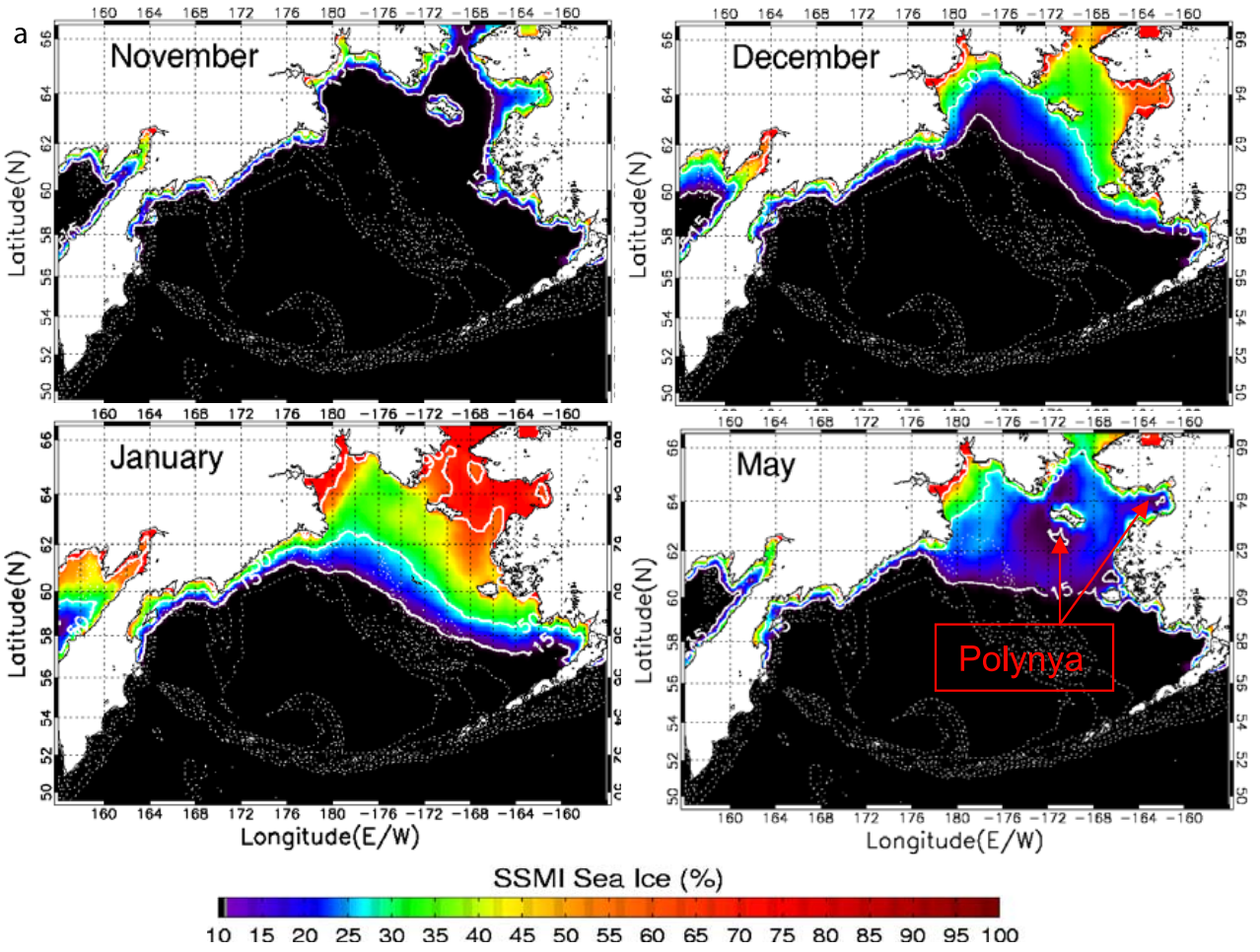

Figure 5. (a) The SSM/I-measured climatology for spatial evolution of SIC for November, December, January (freezeup season), and May (breakup season), averaged from 1996 to 2006. (b) Same as Figure 5a except for the CIOM-modeled SIC using NCEP daily climatological atmospheric forcing averaged from 1996 to 2006.

[20] After a 6-year spin-up using NCEP monthly climatology, a dynamical and thermodynamical seasonal cycle is established. Then, we reran the model for another 4 years using the previous sixth-year output as the restart or initial conditions. During the 4-year run, the climatological daily atmospheric forcings derived from the NCEP Reanalysis for period 1996–2006 were used to drive the model. Then, the last year variables were used for examining the seasonal cycle in this study.

3. Results

3.1. Sea Ice Temporal and Spatial Variability

[21] A seasonal cycle of sea ice cover (area) is an important parameter to be examined because there are sufficient satellite measurements to validate the CIOM's performance. The Bering Sea ice is first-year ice and is free of ice in summer. Ice cover usually reaches its maximum in February that remains from March to April and starts to melt in late April. Figure 3 shows the simulated March SIC (Figure 3a), the SSM/I measurement (Figure 3b), and simulated sea ice thickness superimposed by ice velocity (Figure 3c). Overall, the spatial pattern of the model-simulated SIC is consistent with the satellite measurement, except along the Siberian coast where the model reproduces less ice. The ice edge elsewhere compares well to the observation. This large discrepancy may be due to (1) a possible overshooting of the Bering Slope Current that advects excessive heat from the eastern Bering Sea to the west coast and (2) a systematic error in satellite-measured sea ice extent. We found that along the coast, satellite-measured sea ice extent is overestimated by 10–15% yearlong because of sea fog, particularly in summer. One important feature of the model simulation is that there are sizable ice floes, whereas the SSM/I ice map does not capture this feature. This may be due to the fact that the Bering-CIOM has a relatively high resolution compared to the SSM/I resolution (25 km) and other global climate models [*Watanabe et al.*, 2006], which cannot capture the sea ice dynamics. The simulated sea ice velocity field (Figure 3c) shows that strong northeasterly wind drives sea ice southwestward with a typical magnitude of ~15 cm/s. The averaged ice thickness is about 0.4 m, comparable to the satellite estimate of 0.43 m [*Tateyama and Enomoto*, 2001]. Polynyas are found in the Northern Gulf of Anadyr, Eastern Norton Sound, near Cape Prince of

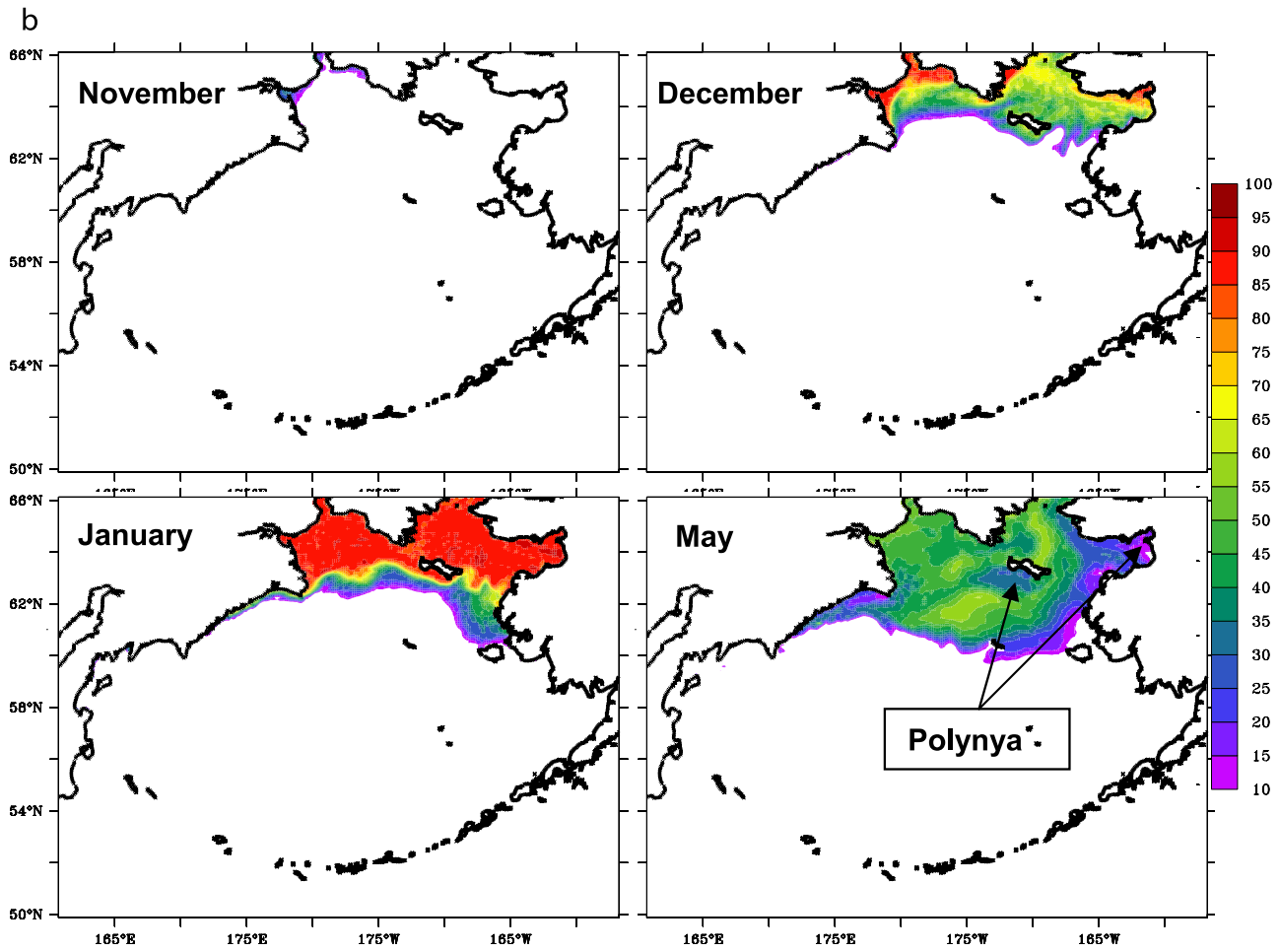

Figure 5. (continued)

Wales, and the lee side (south) of St. Lawrence Island. Obviously, strong northeasterly wind is the major forcing.

[22] Figure 4 shows the simulated seasonal cycle of Bering Sea ice area against the daily satellite measurements with the systematic error removed because of coastal sea fog. The simulated maximum sea ice area of 0.55×10^6 km^2 is in late March and early April, while the SSM/I-observed maximum is in February and in mid-March to April. Although the model does not capture the peak in February, the overall seasonal cycle was reasonably reproduced, except that the sea ice melting from March to April is slower than the SSM/I measurements.

[23] The spatial pattern of seasonal freezeup and breakup can be measured by the satellite (Figure 5a) and simulated by the Bering-CIOM (Figure 5b). Note that satellite-measured sea ice extent contains a large systematic error along the coast due to sea fog and thus overestimates ice extent by 10–15%. The qualitative comparison between Figures 5a and 5b is encouraging. The SSM/I measurements (Figure 5a) show that sea ice starts to form in November. Sea ice extent accelerates its expansion from November to December; the entire northern Bering Sea is ice covered. Sea ice extent continues to expand from December to February, and reaches a maximum in February–March (see Figure 3). In early April, sea ice extent usually remains steady. Breakup occurs in late April because of increasing daylight length and solar heating. In May, sea ice drastically melts down very quickly; except in the Gulf of Anadyr and in the Bering Strait where SIC is ~50%, the rest of the northern Bering Sea SIC reduces to 10–30%. In June, sea ice extent (not shown) is similar to the November conditions. Polynya exists south of St. Lawrence Island, consistent with historical measurement [*Grebmeier and Cooper*, 1995].

[24] The CIOM-simulated SIC maps (Figure 5b) show larger spatial variability and finer structures than the SSM/I maps. In November, sea ice starts to form from the Gulf of Anadyr. The reason is that the strong northeasterly wind blows away newly formed sea ice along the Alaskan coast, while retaining sea ice along the west coast. In December, sea ice expands from northwest to south. Higher SIC along the west coast than along the east coast also indicates the northeasterly wind effect. There is a polynya in the northern Bering Sea. In January, sea ice extent continues to expand. There is large spatial variability in SIC throughout the winter. In May, the sea ice edge retreats from southeast to northwest because of both thermodynamic and wind forcings. Polynyas are found in Norton Sound and south of St. Lawrence Island, consistent with the satellite measurement (May, see Figure 5a).

[25] It should be pointed out that the simulated polynyas are qualitatively consistent with historical observations

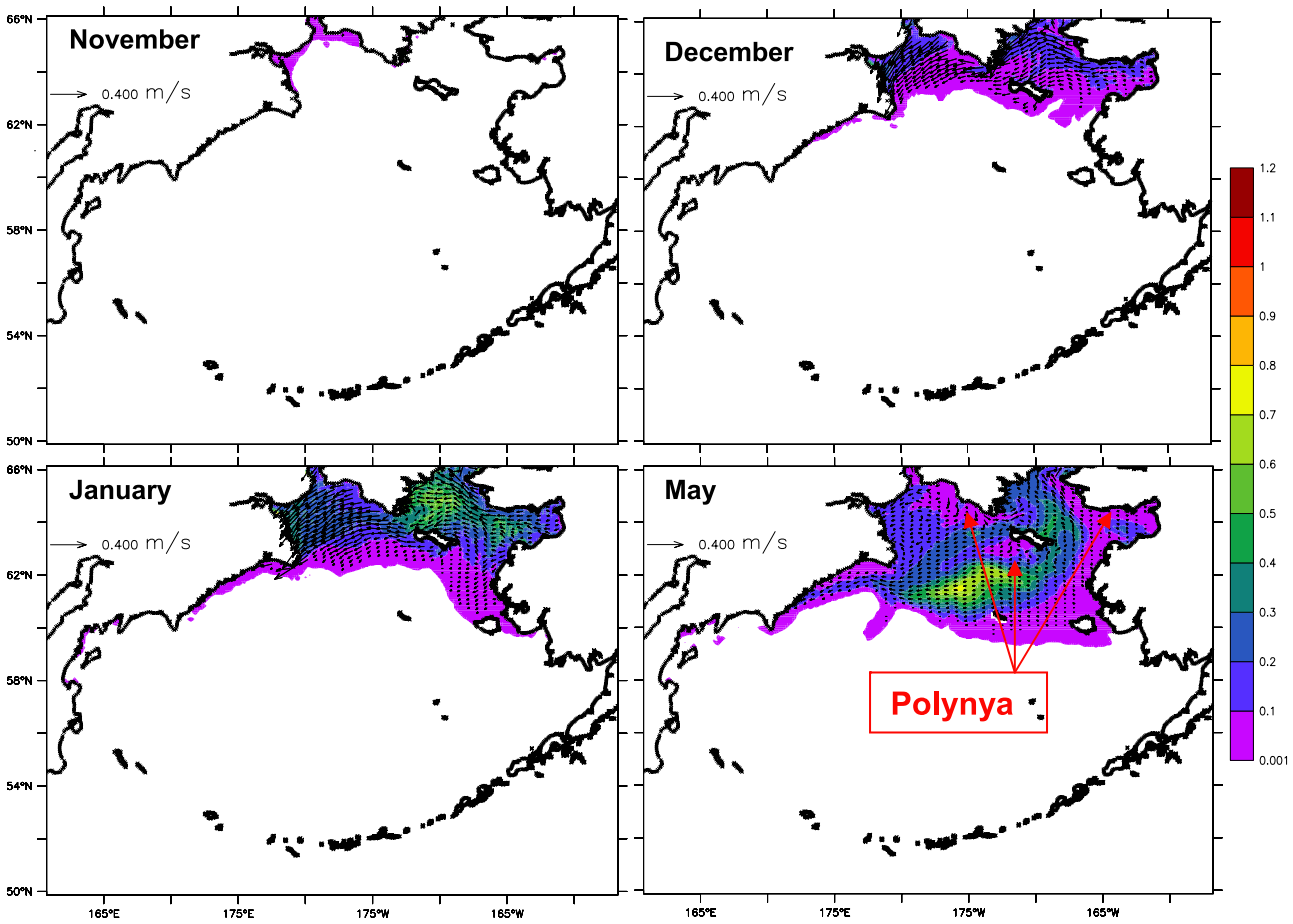

Figure 6. The Bering-CIOM simulated sea ice thickness in November, December, January, and May. Sea ice velocity is superimposed in the thickness map.

summarized by *Niebauer et al.* [1999, Figure 4] on the basis of previous measurements of *Stringer et al.* [1982]. A number of polynyas were observed in the northern Bering Sea: the Gulf of Anadyr including Cape Dezhneva, Norton Sound including Cape Prince of Wales, coast of Seward Peninsula, south of St. Lawrence Island, St. Mathew Island, Nunivak Island, and Yukon Delta coast. The Bering-CIOM can capture some regions with observed polynyas, as discussed above. Nevertheless, year-to-year variability of polynya's location and timing deserves further observational

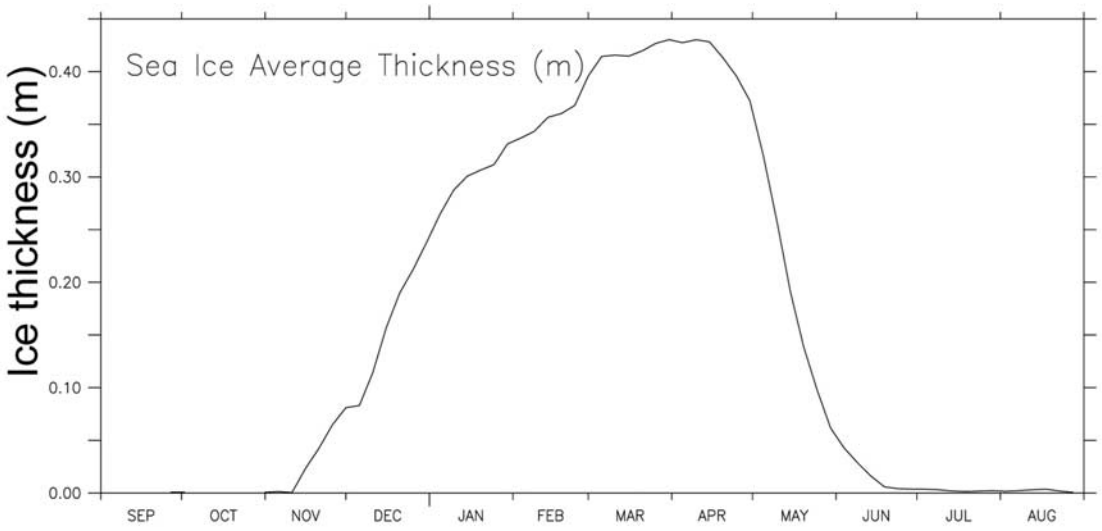

Figure 7. The Bering-CIOM simulated seasonal cycle of domain-averaged sea ice thickness.

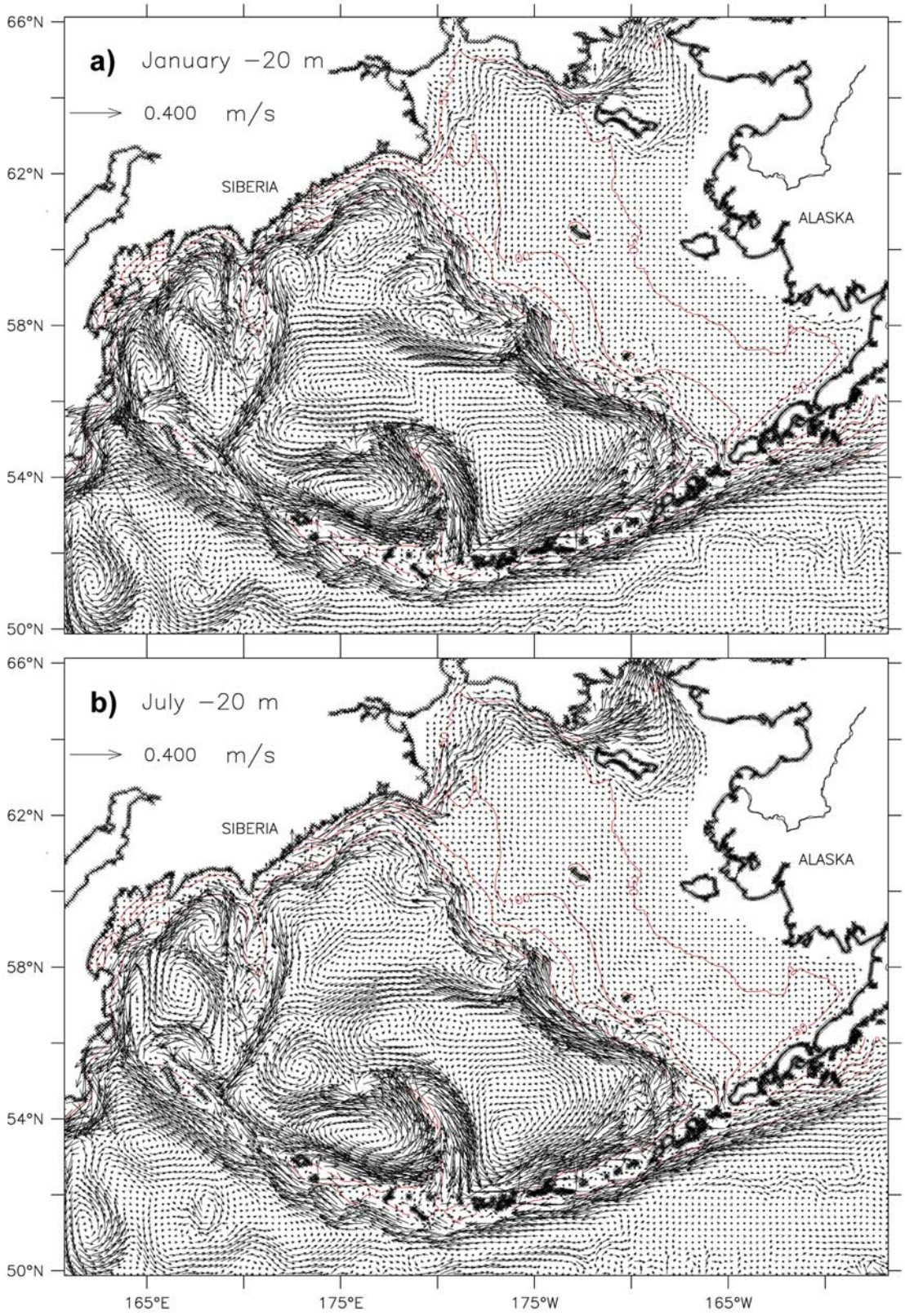

Figure 8. The Bering-CIOM simulated averaged 20-m ocean velocity fields in (a) January and (b) July. The orange lines denote isobaths of 50, 100, 200, and 1000 m.

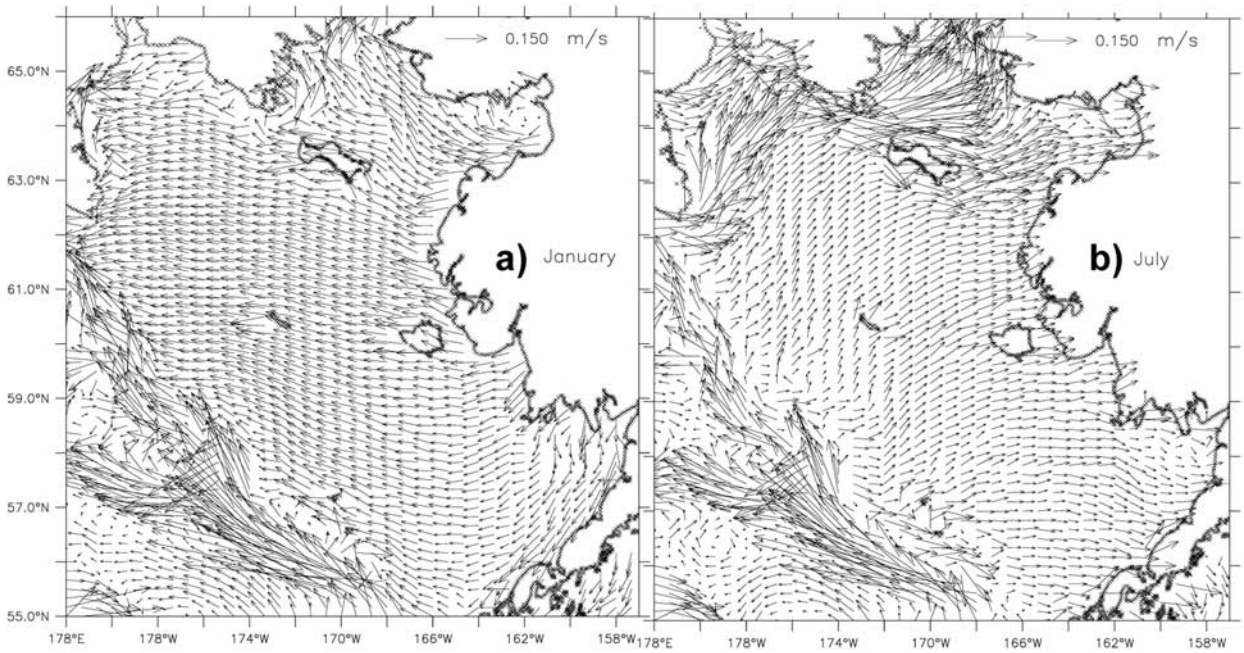

Figure 9. The Bering-CIOM simulated surface current field on the Bering shelves in (a) January and (b) July. Note that the two distinct surface current patterns are due to both the surface wind forcing (Figure 2) and Pacific-Arctic pressure head.

and modeling studies because polynyas can significantly modify the physical environment [*Cavalieri and Martin*, 1994] and ecosystems [*Grebmeier and Cooper*, 1995]. A large polynya was measured in the melting season near St. Lawrence Island by the high-resolution satellite measurement (L. McNutt, personal communication, 2006; see also http://www.beringclimate.noaa.gov/essays_mcnutt.html).

[26] Figure 6 shows the spatial distribution of simulated sea ice thickness from November to May. A polynya exists in the northern Bering Sea in December, consistent with the SIC map (Figure 5b). Ice thickness continues to increase from January to March (Figure 3c). During ice melting season in May, there is a polynya south of St. Lawrence Island, while St. Lawrence Island acts as barrier for accumulating sea ice on its upwind (north) side. Sea ice velocity tends to southwestward because of northeasterly wind forcing. Typical ice velocity is about 10–20 cm s^{-1}. Figure 7 shows a seasonal cycle of domain-averaged ice thickness. The thickness is about 0.41 m in late March to early April, and starts to reduce in late April. The domain-averaged ice thickness over the period of February to April is about 0.38 m, which is smaller than the value of 0.41 m estimated on the basis of remote sensed data during the 1990s [*Tateyama and Enomoto*, 2001].

3.2. Ocean Circulation

3.2.1. General Circulation Pattern

[27] Figure 8 shows the summer (July) and winter (January) 20-m ocean circulation patterns. The simulated 20-m circulation reproduces many current system features as observed (see Figure 1) [see also *Stabeno et al.*, 1999, Figure 10] in literature, such as the Anadyr Current, Bering Slope Current (BSC), East Kamchatka Current (EKC), Kamchatka Current (KC), North Aleutian Slope Current (NASC), and Alaskan Stream. The distinct difference between winter and summer is that the Anadyr Current is much weaker in winter than in summer. Both the winter and summer velocity fields in deep basins show the strong topographic steering effect, such as along the Bering Slope, Shirshov Ridge, and Bowers Ridge. In the northern Aleutian Basin, there exist seven large eddies, cyclonic and anticyclonic. In the eastern Aleutian Basin no mesoscale eddies are reproduced because the 9-km grids are not eddy admitting, while *Hermann et al.* [2002] and *Mizobata et al.* [2006, 2008], using eddy-admitting (4–5 km) grids, can reproduce propagation of these mesoscale eddies. In the Kamchatka Basin, several large eddies are active.

[28] Because the sea level pressure patterns change significantly from season to season, a low (high) center near the Aleutian Islands in winter (summer) with spring and autumn being transition period [see *Wang et al.*, 2004b, Figure 3], the surface wind fields in winter and summer are basically opposite in direction (see Figure 2). The winter northeasterly wind blows against the Pacific-Arctic pressure head that drives the Bering Sea flow into the Arctic [*Woodgate et al.*, 2005]. The summer southwesterly, although weaker than the winter northeasterly in magnitude, blows favorably along the Pacific-Arctic pressure head. Therefore, the two seasonal wind patterns should produce two distinct surface current patterns, particularly on the shelf regions. Figure 9 shows winter and summer surface current patterns in the Bering Sea shelves. The two shelf current patterns differ distinctly in many ways. First of all, the surface Anadyr Current in summer is much stronger than in winter. The second feature is that the summer (winter) surface current flows northeastward (northwestward) in the northern shelf and eastward (westward to southwestward) in the eastern shelf. The third noticeable feature is that the surface

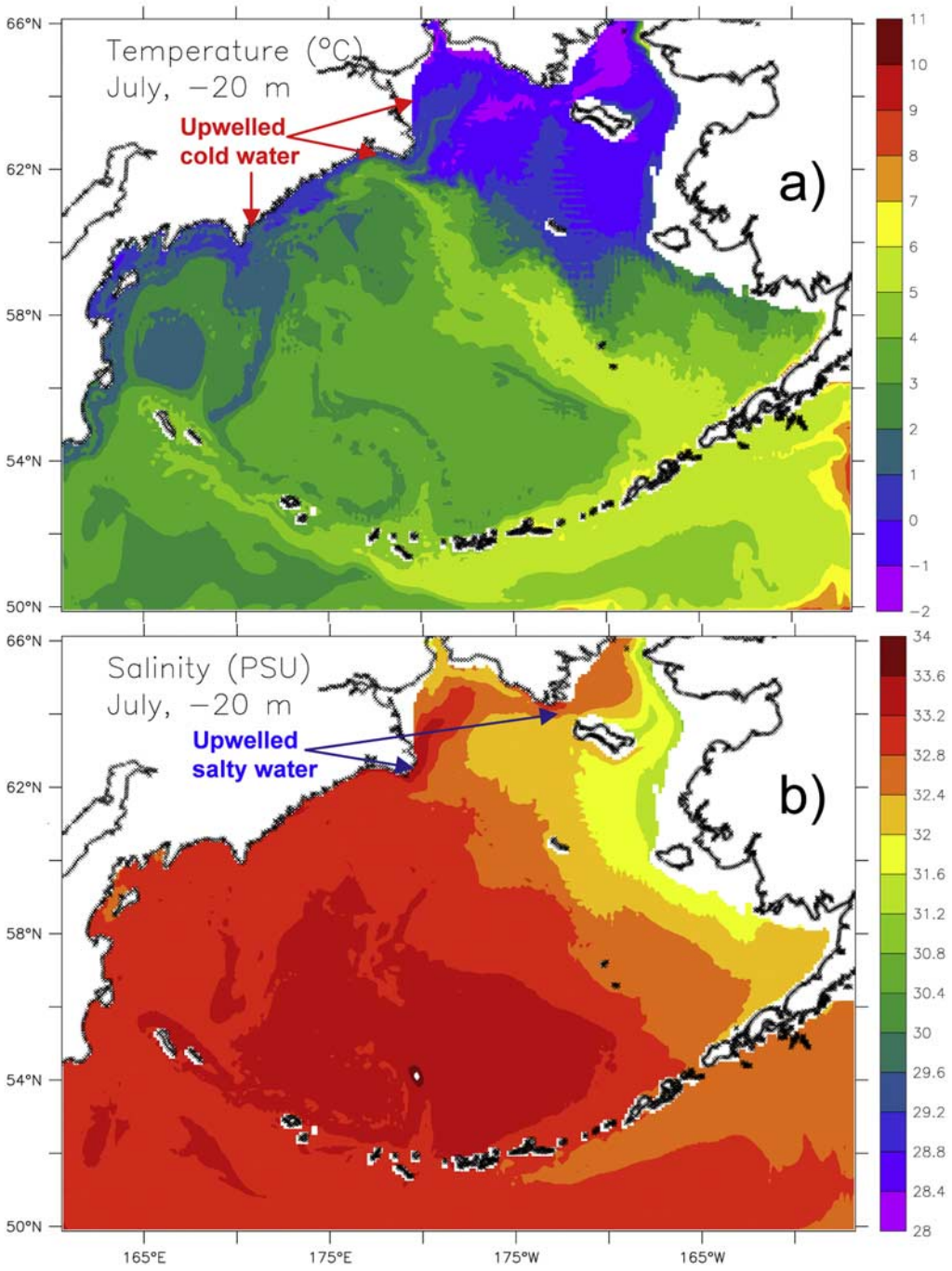

Figure 10. The Bering-CIOM simulated July 10-m ocean (a) temperature and (b) salinity. Note that the Anadyr Current advects warmer and saltier water, while the ACC advects fresher water northward.

ACC flows northeastward in summer, while it flows southwestward in winter. Thus, these two distinct seasonal shelf current patterns result from the combined forcing of seasonally variable Pacific-Arctic pressure head and two distinct wind fields that are opposite in direction.

[29] Figure 10a shows the simulated 20-m ocean temperature field in summer. The warm water is spread from the Bering Slope Current to the East Kamchatka Current, advecting the eastern Bering water mass to the northwestern Bering Sea. It is also evident that the Anadyr Current advects warm BSC water northward along the Siberian coast. Another branch separated from the Bering Slope Current that advects heat northwestward can be seen in the middle of the Bering shelf from Pribilof Island to St. Mathew Island. This branch is still visible in winter (not shown). In winter, the whole Bering shelf experiences a cooling process due to ocean heat loss to the atmosphere. Therefore, the northward advection of the ocean heat flux is much weakened along both the Alaskan Coastal Current and the Anadyr Current. A striking feature is that along the

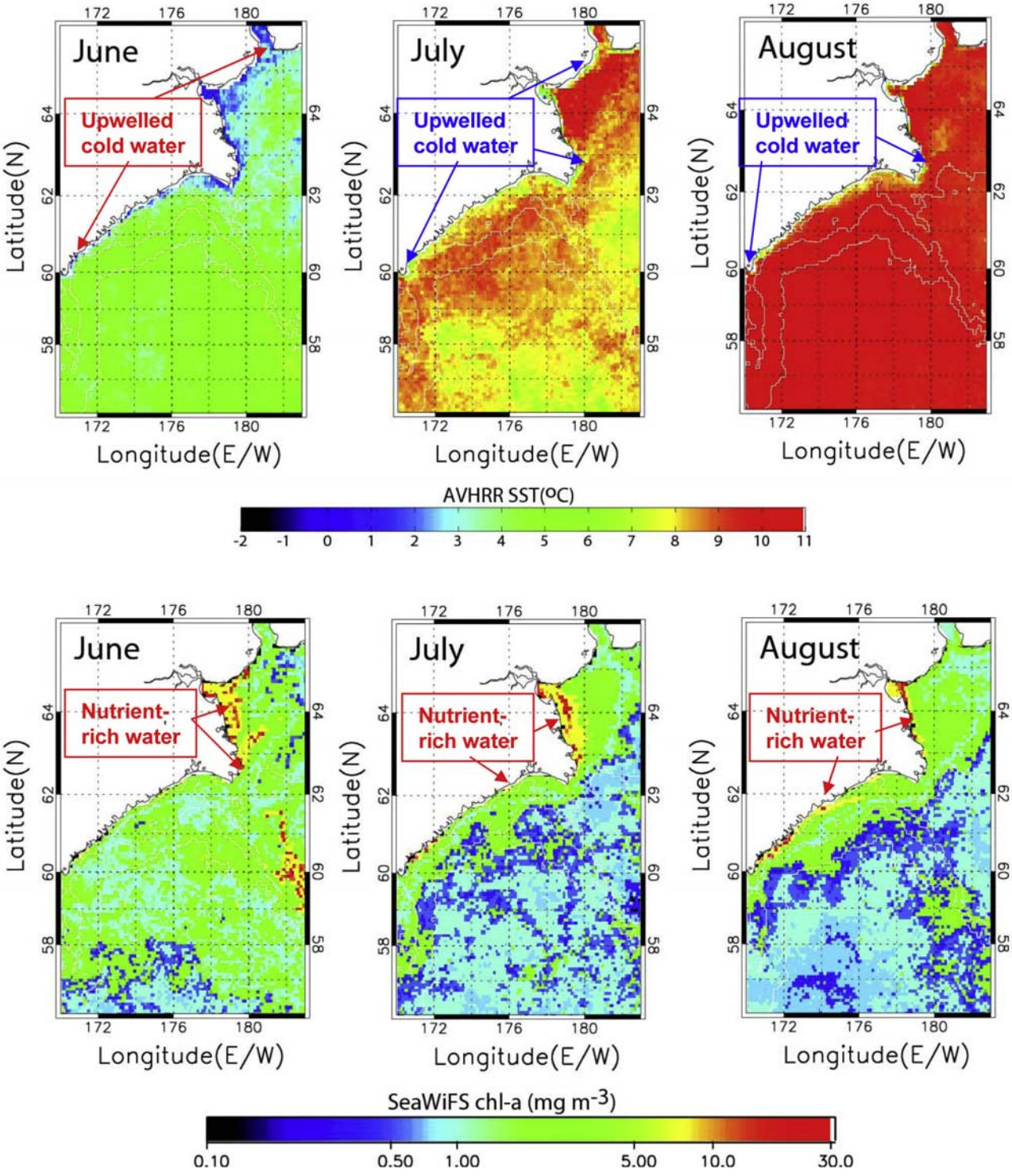

Figure 11. The (top) 4-km AVHRR-measured SST climatology and (bottom) 10-km SeaWiFS-measured chlorophyll-a climatology in June, July, and August averaged from 1996 to 2006. The upwelled cold water is marked. Superimposed are depth contours of 100, 1000, and 3000 m.

western coast near Cape Navarin, there exists a narrow strip of cold water, compared to the warm Bering Slope water and to the surrounding waters. This indicates an upwelling due to a basin-scale surface Ekman drift (Figure 9b) driven by the large-scale wind field (Figure 2b). A similar upwelling (i.e., cold water) also occurs along the coast of Gulf of Anadyr, consistent with the results of *Nihoul et al.* [1993].

[30] The modeled 20-m ocean salinity fields (Figure 10b) shows that the ACC in summer advects fresher water northward in the eastern Bering Sea, while the Anadyr Current transports saltier water masses northward along the western coast. The freshwater transport by the ACC originates from the AS water via Aleutian passes and river runoff from Alaskan watersheds, such as Kuskokwim and

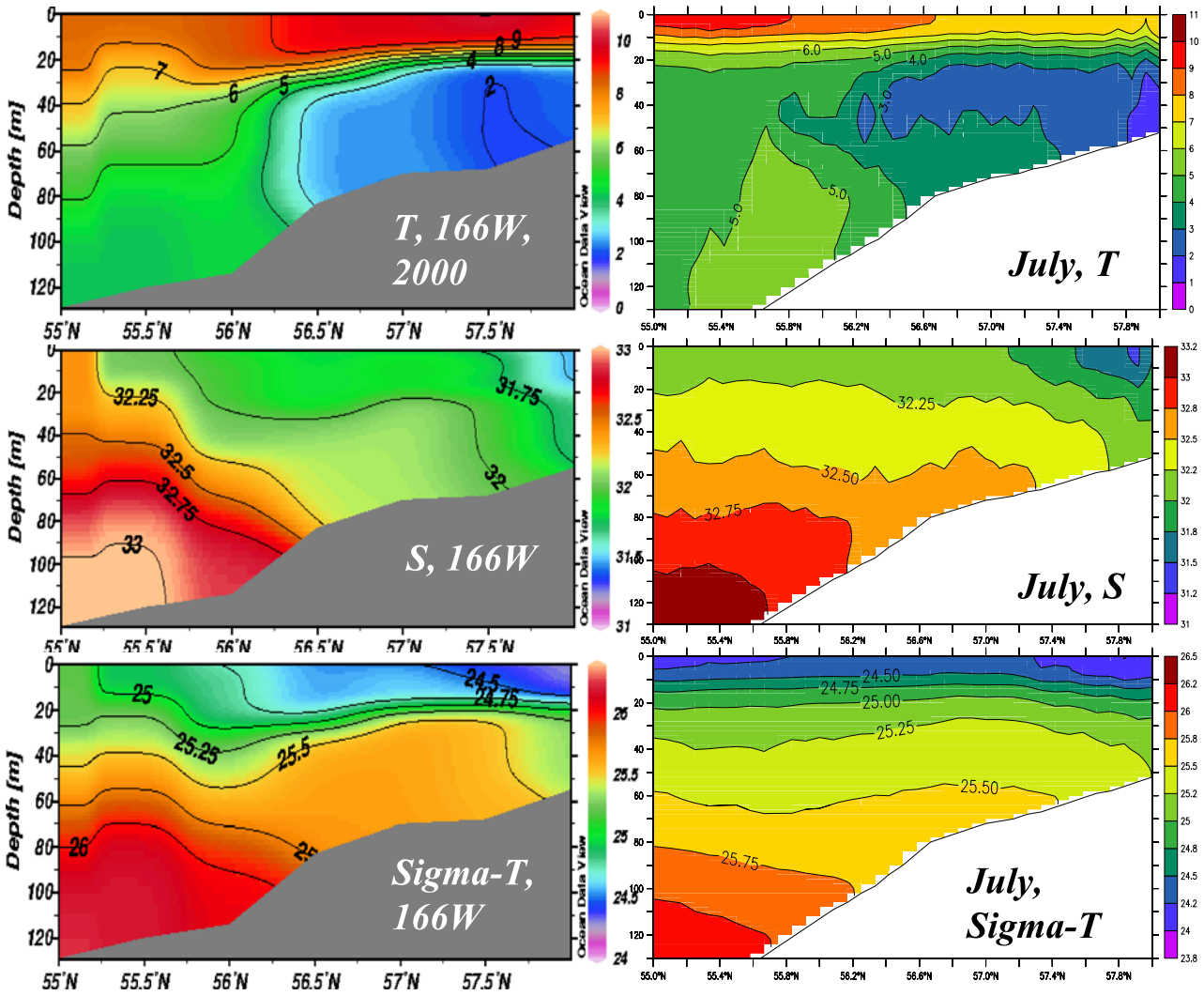

Figure 12. The comparison between (left) the in situ measurements in July 2000 by T/S *Oshoro-maru* and (right) the Bering-CIOM simulations.

Yukon rivers. Along the western coast, corresponding to the upwelled cold water, there exists a narrow strip of high-salinity water compared to its surrounding water. Along the western coast of the Gulf of Anadyr, in particular near Cape Dezhneva, the water with high salinity is captured. The cold, salty water mass along the western coast (near Cape Navarin and Cape Dezhneva) must originate from the subsurface water, because the surrounding waters are warmer and fresher. *Nihoul et al.* [1993] also captured an upwelling in the Gulf of Anadyr, the downstream of the Anadyr Current, using both model simulations and satellite measurements, which does bring up cold, nutrient-rich water from the subsurface to the surface.

[31] To investigate and confirm this upwelling, the SST maps from the AVHRR (Advanced Very High Resolution Radiometer) were collected and analyzed. We examined the summer (June, July and August) AVHRR data from 1996 to 2006. It was concluded that this narrow upwelling along the Siberian coast is a ubiquitous phenomenon and appears almost every year, although there is significant interannual variability. Figure 11 (top) shows the climatological SST maps in June, July, and August averaged from 1996 to 2006. In June, there was a narrow band of cold (~2–3°C) water along the western coast (from south all the way to the Gulf of Anadyr), while the water temperature farther offshore was 4–7°C. In July, the cold water band was about 4–6°C, while the ambient water temperature was greater than 8°C. In August, the upwelled cold water was still visible; the nearshore SST was 7–8°C, while the ambient SST was higher than 10°C. In particular, off Cape Navarin, the SST was around 7°C, while the Anadyr Current water temperature was greater than 10°C. Along the EKC, the nearshore SST was 7–8°C, while the EKC water farther offshore was greater than 11°C. Along the western coast of the Gulf of Anadyr, a similar cold water mass is also found in the SST maps from June to July, while in August, the upwelling (cold water) usually weakens or disappears.

[32] To further validate the finding that this upwelling brings up the subsurface nutrients to the surface that feed phytoplantons, we analyzed chlorophyll-a data measured by SeaWiFS (Sea-viewing Wide Field-of-view Sensor). Figure 11 (bottom) shows the climatological chlorophyll-a of June, July, and August averaged from 1996 to 2006. In June, there exists strong phytoplankton blooms (chl-a > 9 mg m^{-3})

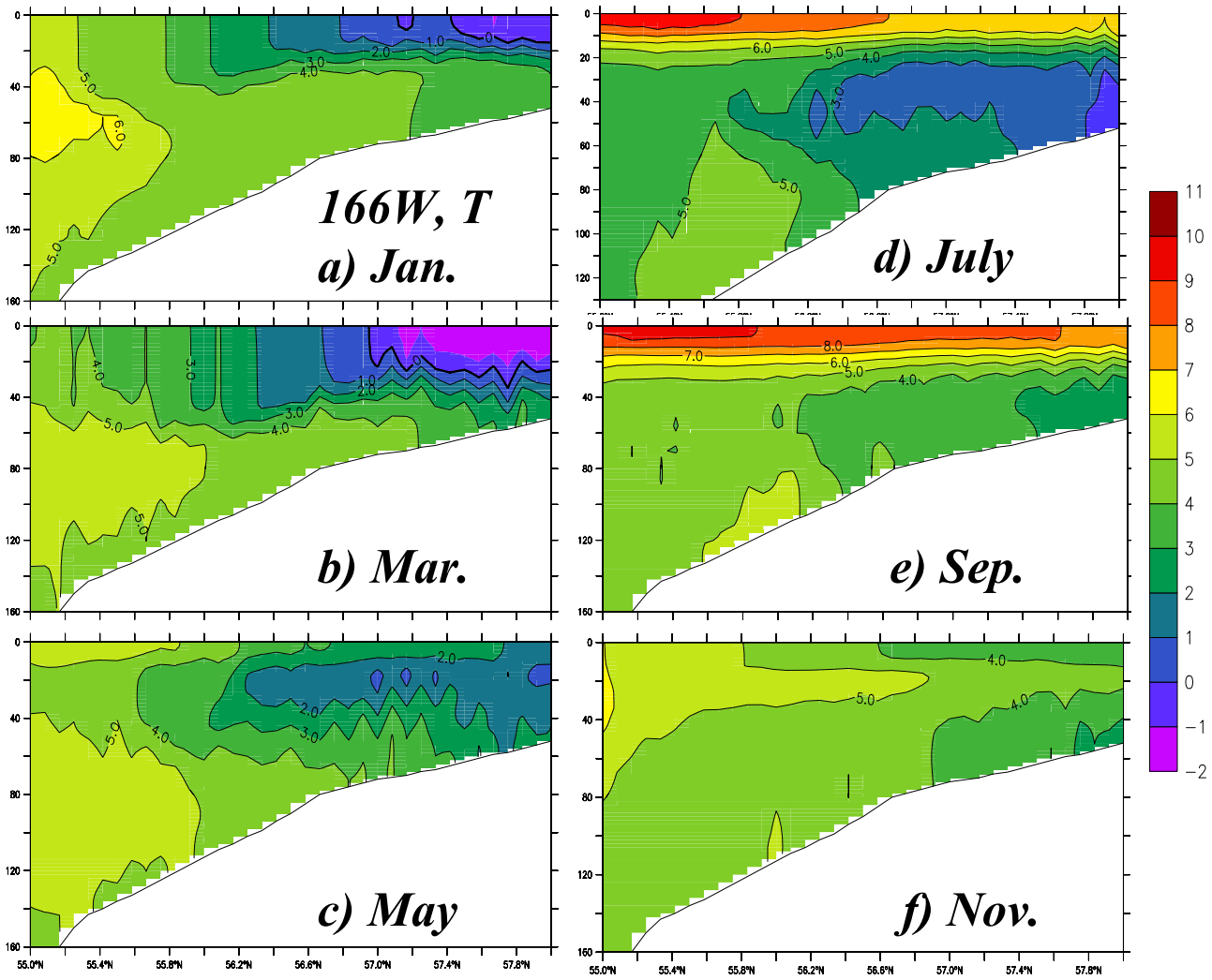

Figure 13. The Bering-CIOM simulated the evolution of bimonthly ocean temperature along the 166°W line.

along the BSC that is the so-called the Green Belt [*Springer et al.*, 1996]. Along the western coast of the Gulf of Anadyr, strong phytoplankton blooms (chl-a > 8 mg m^{-3}) occur, which must be due to the strong upwelling. South of Cape Navarin, there were no significant blooms. In July, there were high concentrations south of Cape Navarin and in the Gulf of Anadyr. The blooms were persistent throughout August. The distinct difference between the upwelling-led phytoplankton blooms and the Green Belt blooms is that the former occurs along a nearshore narrow strip with higher chlorophyll-a concentration (>8 mg m^{-3}), while the latter occurs offshore with a broad belt with chlorophyll-a concentration between 2 and 7 mg m^{-3}. Thus, the upwelling exists during summer that is accompanied by high chlorophyll-a concentration (i.e., phytoplankton blooms) due to vertically advected nutrient-rich water from the subsurface.

3.2.2. Bering Shelf Dynamics: Vertical Structure and Transports

[33] In the southeastern Bering shelf, annual hydrographic survey during July–August is conducted by the Hokkaido University T/S *Oshoro-maru*. A long-term CTD survey along the 166°W line between 55 and 58°N has been maintained since 1994 (Figure 1 for location), although the survey arrays (stations) vary from year to year. The survey was conducted only in summer. Nevertheless, these observations can help reveal the seasonal cycle of this section with the help of the Bering-CIOM.

[34] Figure 12 shows the *Oshoro-maru* measurements along the 166°W line in July 2000. The measurements show a water with minimum temperature of <2°C lies on the shelf, which is the winter water formed because of vertical convection. The upper mixed layer depth is about 20–30 m, consistent with the model results (Figure 12, right). The measured salinity distribution along the transect indicates fresh water in the shallow shelf, as reproduced by the model. The shelf break saline water occupies the deeper shelf that may be advected to the shelf depending on mesoscale eddy exchange [*Mizobata et al.*, 2006, 2008] and wind conditions. The density distribution mimics the salinity.

[35] Figure 13 shows the bimonthly ocean temperature distribution. In January, the upper mixed layer of 20–40 m is a result of cooling since the previous autumn. The upper mixed layer deepens in February (not shown), March (40–

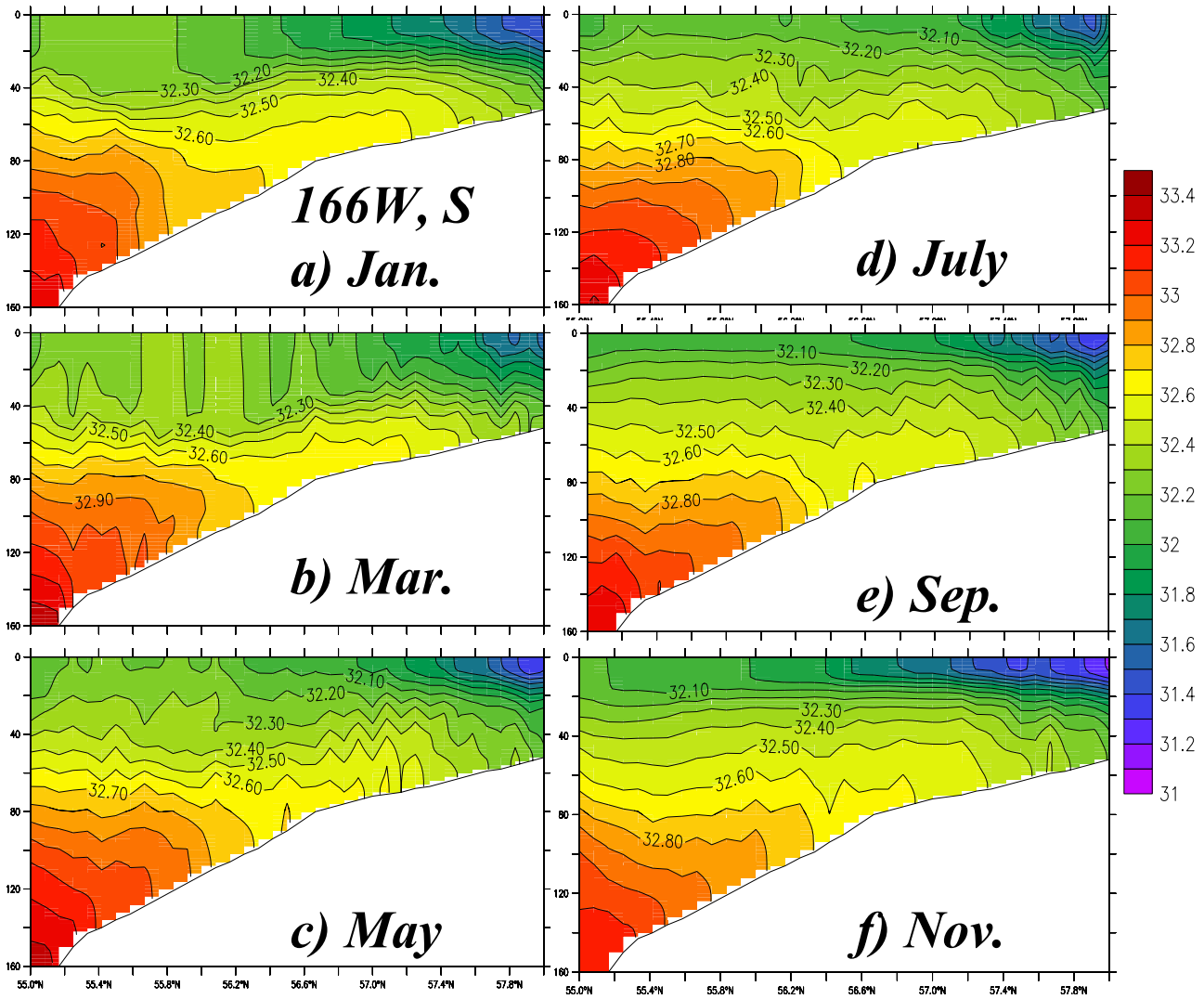

Figure 14. The same as Figure 13 except for salinity.

50 m), and reaches the maximum in April (50–60 m, not shown). Because of increasing solar radiation, surface temperature starts to increases from April through May (Figure 13). The surface thermocline layer starts to form in July with a large vertical gradient. In July, the winter water with a minimum temperature of 2°C stays on the shelf. The summer upper mixed layer reaches a maximum of 20 m in August–September because of wind-wave mixing [*Hu et al.*, 2004], which was underestimated by other models without wind-wave mixing [*Hermann et al.*, 2002; *Clement et al.*, 2005]. In November, the ocean surface is cooled, while leaving a subsurface maximum temperature. This phenomenon should be detected if moorings are in place over the winter. However, *Hermann et al.* [2002] and *Clement et al.* [2005, Figure 10] cannot reproduce this subsurface maximum temperature in November.

[36] Bimonthly salinity distribution along the 166°W line (Figure 14) shows salinity seasonal cycle. The winter upper mixed layer forms in autumn and reaches a depth of 30–40 m in January, and a maximum depth of 40–60 m in March. In May, because of sea ice melting and coastal river runoff, spring freshening occurs. In July, a strong upper halocline forms. The summer upper mixed layer depth reaches 20 m. In November, the surface salinity increased because of sea ice formation, leading to a well mixed water column.

[37] The vertical distribution of E–W component of current (Figure 15) indicates strong baroclinicity. In January, a northwesterly wind (Figure 2a) drives the surface current westward (Figure 9a), while the subsurface currents are eastward. In July, the southwesterly wind (Figure 2b) transports the surface water eastward (Figure 9b), while there are westward currents beneath the eastward surface current. These baroclinic features may be due to the surface Ekman drift and throughflows via Aleutian passes [*Stabeno et al.*, 2005; *Mizobata et al.*, 2008] driven by the Pacific-Arctic pressure head that drives the Bering inflow to the Arctic Ocean [*Woodgate et al.*, 2005].

[38] The north–south transport on the Bering shelf is not only important for the volume transport per se, but also for the north–south connection between the Bering and Chukchi ecosystems. *Springer and McRoy* [1993] show that the Anadyr Current advects warm, salty, nutrient-rich water into the Chukchi Sea on the western side of the Bering Strait,

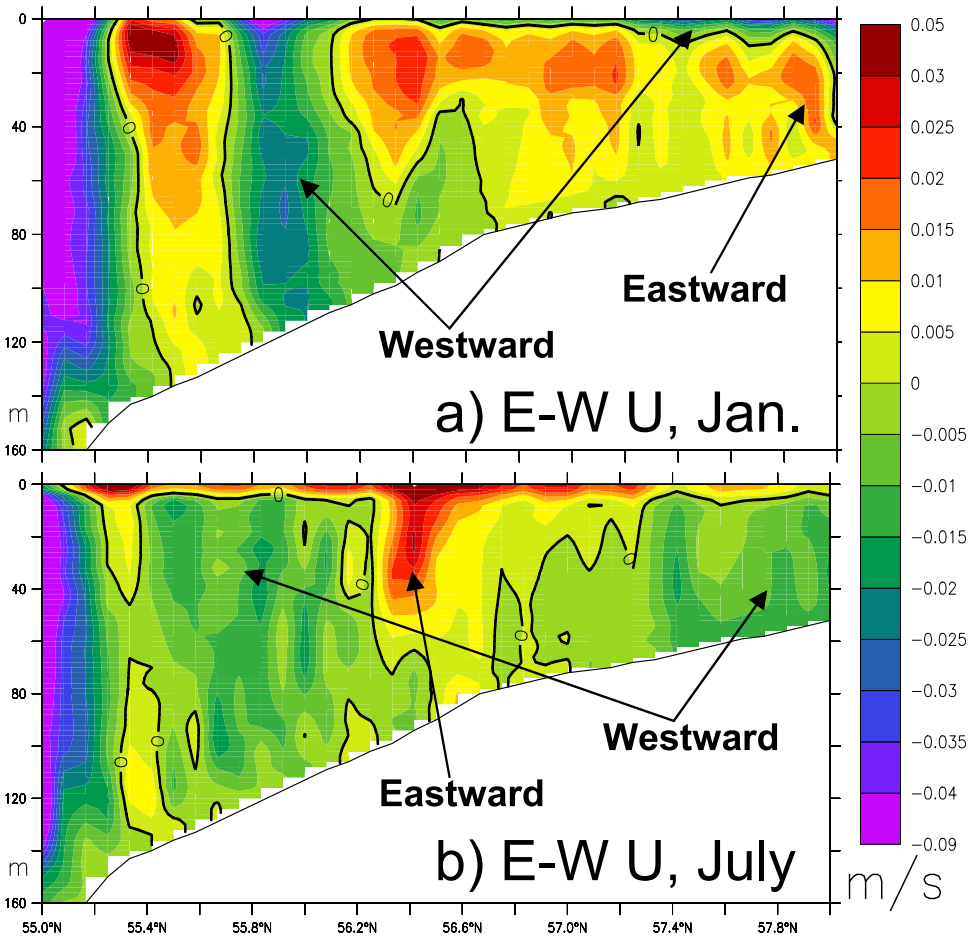

Figure 15. The Bering-CIOM simulated the E–W velocity of (a) January and (b) July along the 166°W line. The positive values are eastward (in red), while negative values are westward (in blue). The zero velocities are denoted by the thick black lines.

while the Alaskan Coastal Current transports fresh, cold, nutrient-poor water to the Chukchi Sea on the eastern side of the Strait. To reveal mechanisms leading to the observed phenomena, the 62.5°N line was selected (see Figure 1 for location) to examine in depth horizontal transports and vertical structures, because this transect can be used to investigate both the Alaskan Coastal Current at the east and the Anadyr Current on the west.

[39] Figure 16 shows the January (winter) and July (summer) temperature, salinity, and the N–S velocity distribution across the 62.5°N line. The winter temperature is well mixed vertically at a freezing temperature, except in the deep western part. The Bering Slope Current is still visible. This locally formed cold water in winter can survive the summer (see July map). This process is very common in the Bering shelf, consistent with available observations in the southeastern Bering shelf [*Kinder and Schumacher*, 1981] (see also Figure 12) and model simulations [*Overland et al.*, 1999]. In July, thermal stratification prevents solar heating from further mixing downward.

[40] Winter salinity distribution indicates strong vertical convection, leading to vertical homogeneous distribution on the shelf. This process is again due to sea ice formation that injects salt to the ocean surface, destabilizing the water column. Two important phenomena can be detected. First, on the western side of the basin, high-salinity water (>33 practical salinity units (psu)) can be found on the slope that is ventilated to the surface, which should result from deep convection due to salt injection when sea ice forms. As a result, dense water forms and descends along the steep slope [*Wang et al.*, 2003b]. The downwelling favorable northeasterly (Figure 2a) promotes this deep convection process. Second, on the eastern side of the shelf, fresh water from Yukon River runoff is advected southward by the southward current (see Figure 9a) due to the northeasterly wind (Figure 2a), because surface-trapped freshwater plumes, in general, follow the wind direction [*Wang et al.*, 1999].

[41] In summer (July), a saline water mass (Figure 16d) that is formed during the previous winter lies on the shelf, corresponding to the cold water mass (Figure 16b). In contrast, on the western side, an upwelling is suggested by the upwelled cold, saline water (see Figure 10) due to the basin-wide southwesterly wind (Figure 2b). This upwelling lifts up the nutrient-rich subsurface water with cold and saline property to the euphotic zone, leading to a persistent high-productivity area in the western side of the Bering Sea [*Springer and McRoy*, 1993; *Nihoul et al.*, 1993] (see *Sukhanova et al.* [1999, Figures 1–2] for high phytoplankton blooms). Furthermore, the Anadyr Current advects this nutrient-rich water into the Arctic Ocean via the Bering

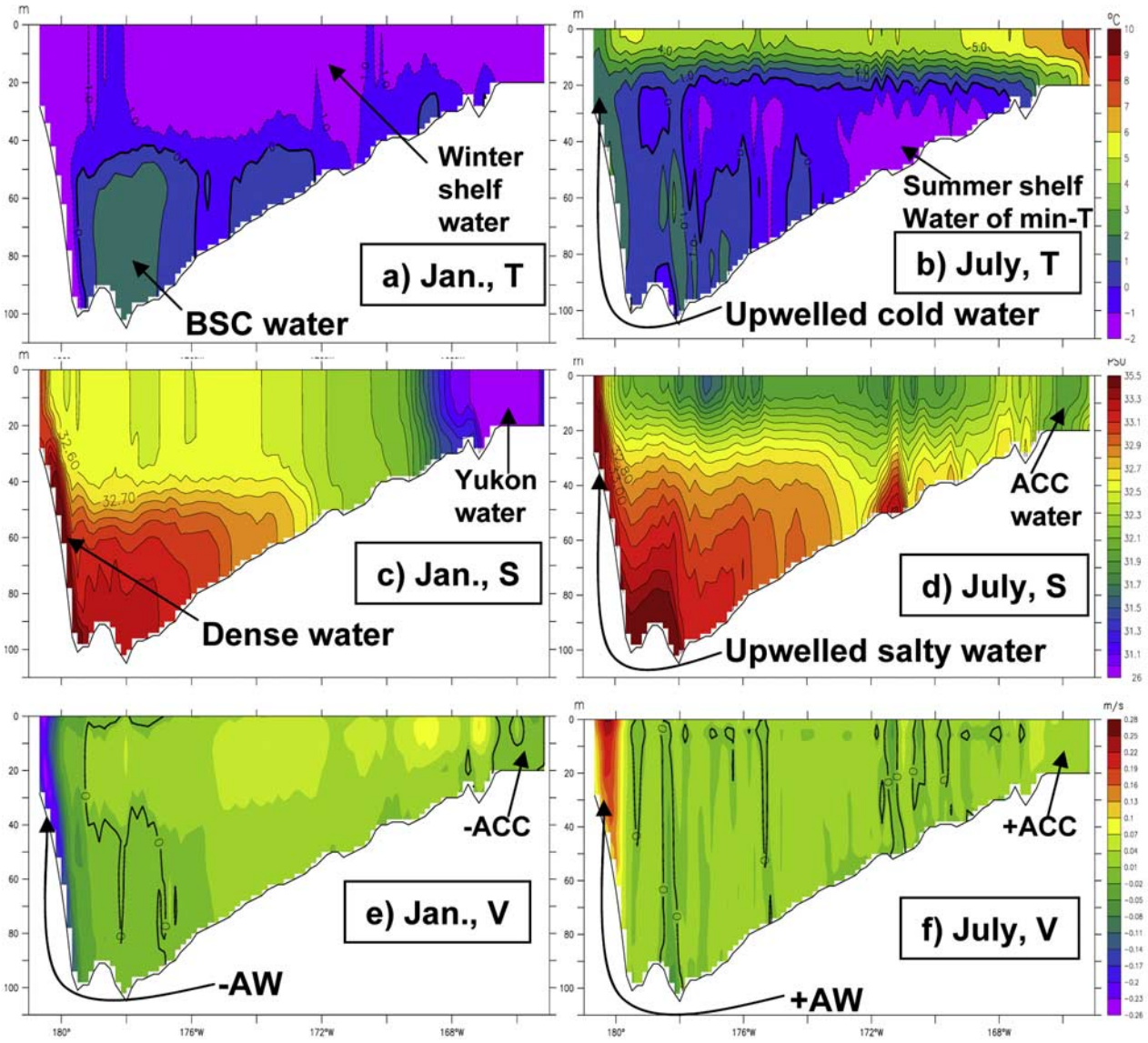

Figure 16. The Bering-CIOM simulated the temperature, salinity, and N–S velocity of (left) January and (right) July along the 62.5°N line. The positive values are northward (in red), while negative values are southward (in blue). The zero velocities are denoted by the thick black lines.

Strait [*Walsh et al.*, 1989]. This is why the Anadyr Current water has higher nutrients than the Alaskan Coastal Current [*Springer and McRoy*, 1993]. On the eastern side of the salinity transect, it is observed that the Alaskan Coastal Current advects relatively low salinity water (relative to the ambient water and to the Anadyr Current water) northward, although it is saltier than the Yukon River runoff.

[42] The velocity distribution (Figure 16) indicates a persistent northward Anadyr Current in summer and reversal transport in winter. The Alaskan Coastal Current flows southward in winter because of the northeasterly wind (see Figure 9a), and northward in summer. In general, the northward transport is fairly barotropic because of no significant vertical structure, which is in contrast to the E–W transport along the 166°W line, where the baroclinic structure is obvious.

[43] Along the 62.5°N line, the volume, heat, and salinity transports were calculated using the following formulas.

$$Q_{volume} = \iint_{xz} v dz dx \qquad (\text{in units of } m^3\ s^{-1})$$

$$Q_{heat} = \iint_{xz} \rho C_p (T - T_{ref}) v dz dx \qquad (\text{in units of watts})$$

$$Q_{salt} = \iint_{xz} (S - S_{ref}) v dz dx \qquad (\text{in units of psu} \cdot m^3\ s^{-1})$$

where v is the N–S velocity, ρ is the water density (kg m^{-3}), C_p is the water specific heat of seawater (3903 J kg^{-1} K^{-1}), T_{ref} is the referenced water temperature,

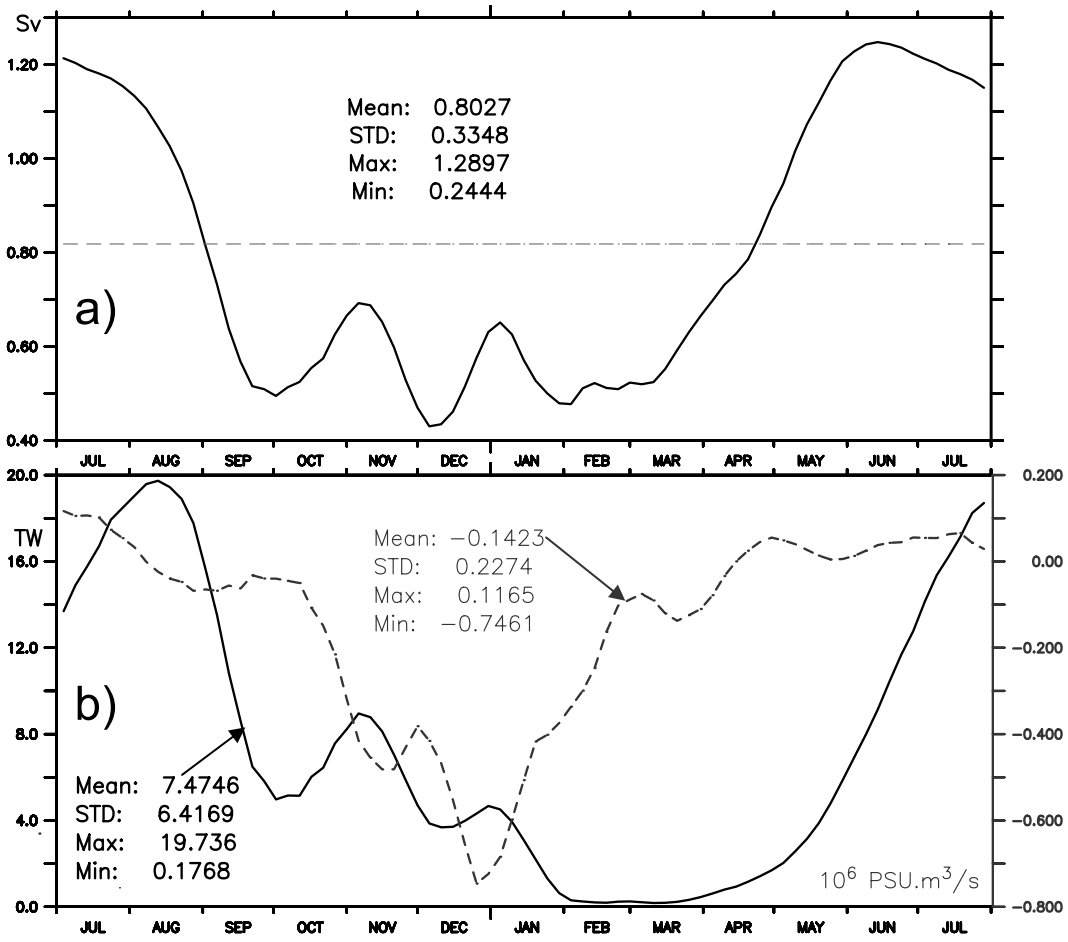

Figure 17. The Bering-CIOM simulated seasonal cycle of (a) volume transport and (b) heat flux (solid line) and salinity flux (dashed line) along the 62.5°N line. The scale for heat flux and salinity flux is plotted on the left and right vertical axis, respectively. The statistics for all the transports are shown as well.

set to be −2°C (0°C = 273.15°K), and S_{ref} is the reference salinity, set to be 32.5 psu on the basis of the observed Bering Slope water (see Figure 12).

[44] Figure 17 shows the annual cycle of the transport with an annual mean 0.80 ± 0.33 Sv. The maximum (minimum) is 1.29 (0.24) Sv in June (December). Relatively small northward transport occurs during the winter months, because the northeasterly wind is against the Pacific-Arctic pressure head [*Woodgate et al.*, 2005]. During the summer, the southwesterly wind is favorable to the Pacific-Arctic pressure head, promoting the northward transport in the Bering shelf, leading to the maximum northward transport (see Figure 9).

[45] The annual mean heat transport across the 62.5°N line is 7.47 ± 6.42 TW. Note that the standard deviation being comparable to the annual mean indicates strong seasonal variation driven by both thermodynamics (sea ice) and local wind forcing. The maximum heat transport (19.74 TW) occurs in August, because the ocean temperature is highest, and the volume transport is high in summer. The minimum heat transport of 0.18 TW occurs in February–March, and heat transport remains low in winter. The heat transport here is depleted for melting local sea ice or/and released to the atmosphere.

[46] Salinity transport across this transect shows the large variation because the standard deviation (0.22) is larger than the annual mean (−0.14), suggesting that the seasonal salinity advection is very complicated. The negative salinity transport of $-0.14 \cdot 10^6$ psu m^3 s^{-1} indicates a northward freshwater transport. The maximum salinity transport (0.12) occurs in July, while the minimum transport with larger magnitude (−0.75) occurs in December. The reason is that the local water, where sea ice formation injects salt to the local ocean surface, is saltier than water coming from the south. Thus, the northward transport advects salty water in summer, while it advects fresh water (negative salinity transport) during winter. Table 1 summarizes the 62.5°N line transport statistics. In summary, the maximum volume and salinity transports occur in June, while the maximum

Table 1. Annual Mean Volume, Heat, and Salinity Transports Along the 62.5°N Line

Annual Statistics	Mean	STD	Maximum/Month	Minimum/Month
Q (Sv)	0.80	0.33	1.29/Jun	0.24/Dec
Q_H (TW)	7.47	6.42	19.74/Aug	0.18/Feb–Mar
Q_S (10^6 psu · m^3 s^{-1})	−0.14	0.22	0.12/July	−0.75/Dec

Table 2. Annual Statistics of the 62.5°N Line Subsections: AC, Midshelf, and ACW[a]

Annual Mean (STD)	AC (Coast–178°W)	Midshelf (178–168°W)	ACW (168°W–Coast)
Q_{VOLUME} (Sv)	0.11 (0.45)	0.62 (0.28)	0.08 (0.08)
Q_{HEAT} (TW)	2.72 (4.03)	3.30. (2.40)	1.50 (1.50)
Q_{SALT} (10^6 psu · m^3 s^{-1})	−0.02 (0.15)	−0.08 (0.11)	−0.05 (0.08)

[a]The numbers in the parentheses are the standard deviations.

heat transport occurs in August, about 2 months later. In contrast, the minimum volume and salinity transports occur in December, while the minimum heat (cold water) transport occurs in February–March.

[47] To further demonstrate the northward transports in different subsections of the 62.5°N line, three sections are selected (see Figure 1 for the sections): the Anadyr Current section that is from the west coast (roughly at 181°W) to 178°W (∼150 km), the midshelf section (178–168°W, ∼500 km), and Alaskan Coastal Water (ACW) section (168°W to the Alaskan coast at about 165°W, ∼150 km). Figure 18 shows the seasonal cycles of individual volume, heat, and salinity transports, which are summarized in Table 2. The annual mean volume transport for the AC, midshelf, and ACW is 0.11 ± 0.45, 0.62 ± 0.28, and 0.08 ± 0.08 Sv, respectively. The AC volume transport has the largest seasonal variation, because the standard deviation (0.45 Sv) is four times the annual mean (0.11 Sv). The AC reaches the maximum northward transport (0.70 Sv) in June and the minimum in December (−0.92 Sv, reversed transport), indicating that the AC is closely related to both the Pacific-Arctic pressure head and winter wind forcing. In contrast, the midshelf volume transport (0.62 Sv) has small seasonal variation (±0.28 Sv) with year-round northward transport, suggesting that the Pacific-Arctic pressure head dominates the northward transport on the broad shelves, while wind-induced transport is secondary. These two transports between the AC and the midshelf are almost out of phase (see Figure 18a). The ACC is dominated by the northward transport (0.08 Sv), except for several reversals, whose seasonal variation is also smaller than the Anadyr Current transport.

[48] Figure 18b shows that the winter heat transport (with an annual mean of 2.72 TW) by the Anadyr Current is also almost out of phase to the midshelf heat transport (with an annual mean of 3.30 TW). The largest Anadyr Current heat transport (9.65 TW) occurs in July–August because the summer Anadyr Current transport is the largest in the three subsections (Figure 18a). Nevertheless, the winter heat transport by the Anadyr Current is southward, because it reverses the direction to southward in winter months. Correspondingly, the midshelf heat transport is northward year round, with a maximum (8.11 TW) in November. Although the Anadyr Current volume transport is only 0.11 Sv, nearly six times smaller than the midshelf transport (0.62 Sv), it transports an annual-averaged heat flux of 2.72 TW northward, comparable to the broad midshelf heat transport (3.30 TW), and larger than the ACC-advected heat transport (1.5 TW). The ACC in general transports heat northward in summer months, while it provides almost no heat transport in winter and spring.

[49] It is found that the Anadyr Current transports salty water northward from May to October (Figure 18c) and fresh water from November to May with a maximum (−0.28) in February. There are two mechanisms at work here: First, if the Anadyr Current volume transport is positive (northward), the advected water from the south is fresher than the local water because the local salinity along the AC region is much saltier because of salt injection from ice formation; second, if the AC volume transport is negative (southward) in winter, it would advect the local high salinity southward. The midshelf circulation transports salinity flux northward during late February to early May (ice melting season) and freshwater during the rest of the year. The ACC contributes significant freshwater northward from late June to January (Figure 18c). Note that the salinity transport by the AC is not in phase with the midshelf circulation and ACC salinity transports; however, the salinity transport by the midshelf and ACC are almost in phase.

4. Conclusions and Discussion

[50] On the basis of the above investigations, the following conclusions can be drawn:

[51] 1. The Bering-CIOM can reproduce seasonal cycles of sea ice cover, thickness, and velocity field. The simulated sea ice area compares very reasonably with the satellite (SSM/I) measurements. Furthermore, the model can capture some downscaling and spatially variable features that the SSM/I measurements cannot. Polynyas were reproduced in the regions where historical observations confirmed their existence. The modeled domain-averaged maximum ice thickness is 0.42 m in March, while the ice thickness averaged over February to April is 0.38 m, compared to the satellite estimate of 0.41 m during the 1990s. The modeled ice thickness shows large spatial variability; nevertheless, the lack of thickness measurements prevents us from validating the thickness distribution.

[52] 2. There are two distinct surface circulation patterns, winter and summer, on the Bering shelves due to Ekman drift. The winter surface current is more or less southwestward or northwestward, while the summer surface pattern is featured by the northeastward to eastward currents. The simulated general circulation patterns in the lower layers mimics the available schematic circulation pattern based on limited measurement. The topographic steering of ocean currents in deep basins are strikingly important. Thus, the detailed, high-resolution topographic data set is very important in future high-resolution model simulations.

[53] 3. The simulated seasonal cycle of temperature and salinity along the 166°W line in the southeastern Bering shelf compared well with the T/S *Oshoro-maru* field measurements. A minimum temperature (<3°C) water mass in summer is reproduced that is right on the shelf, which actually is the winter water produced by local vertical convection. The summer upper mixed layer depth was estimated to be 20–30 m during strong wind-wave mixing. The E–W velocity structure is of baroclinity.

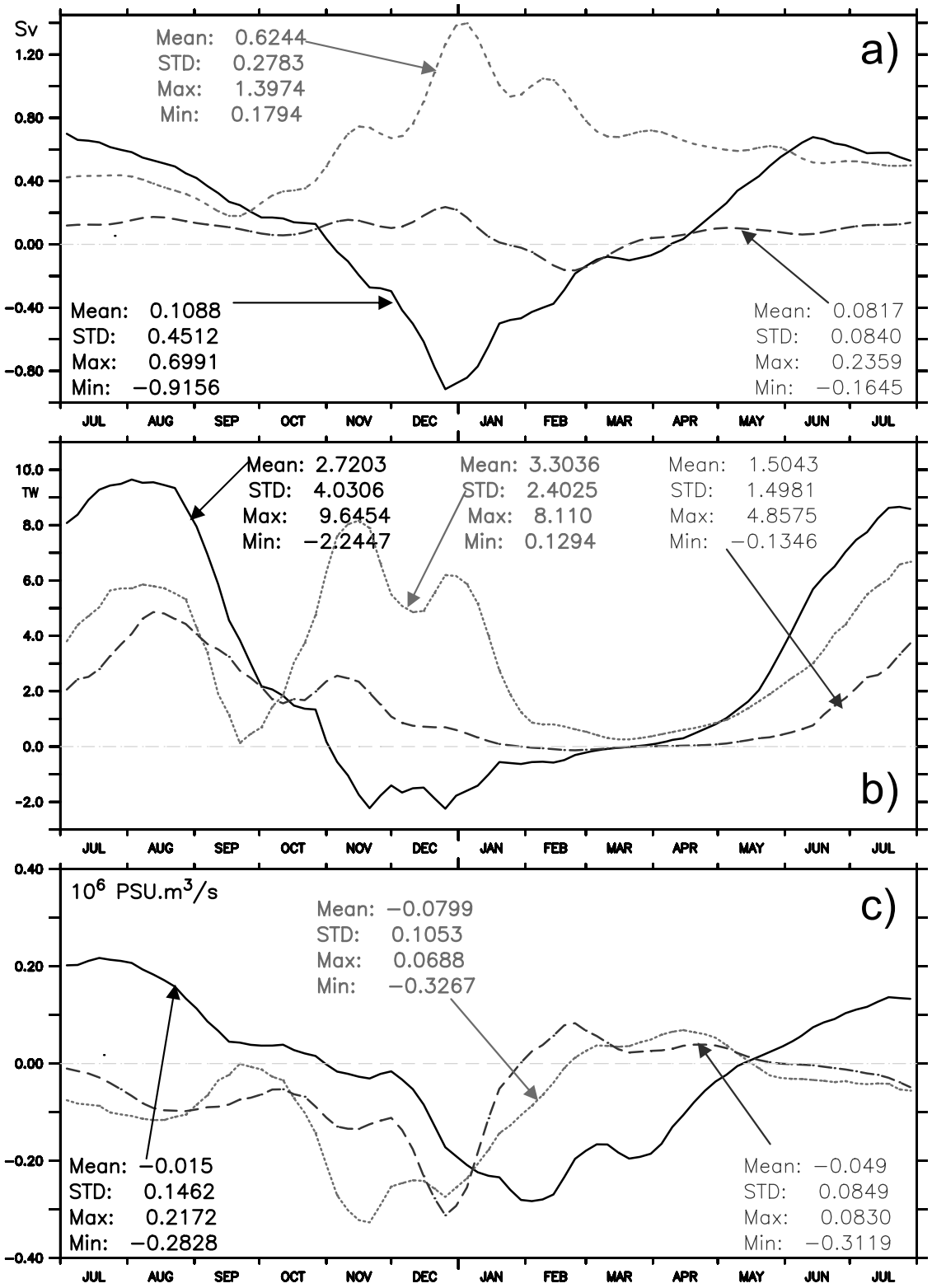

Figure 18. The Bering-CIOM simulated seasonal cycle of (a) volume transport, (b) heat flux, and (c) salinity flux for the three subsections: the AC (solid lines), midshelf (dotted lines), and ACC (dashed lines), along the 62.5°N line. The statistics for all the transports are also shown.

[54] 4. Along the 62.5°N line, there are two different circulation patterns in winter and summer. The winter Anadyr Current has weak northward transport and even reverses its direction to southward because of the weak Pacific-Arctic pressure head and the strong northeasterly wind forcing [*Coachman*, 1993]. This current provides the most heat flux toward the north in summer. The northeasterly produces a downwelling on the western coast that promotes the existing dense water formation (with salinity >33 psu) caused by salt injection due to ice formation. Thus, the winter local salinity along the AC region is saltier than the water coming from the south, leading to negative salinity transport. The summer Anadyr Current is stronger than the winter, where an upwelling occurs, which is driven by the basin-scale upwelling favorable southwesterly wind. Then, the upwelled cold, salty, nutrient-rich water is transported by the Anadyr Current to the Arctic Ocean [*Walsh et al.*, 1989; *Springer and McRoy*, 1993].

[55] 5. Across the 62.5°N line, the maximum volume and salinity transports occur in June and July, respectively, while maximum heat transport occurs in August. The minimum volume and salinity transport occurs in December, while the minimum heat transport occurs in February–March. In winter, the northward volume transport advects relatively small heat flux, and negative salinity flux (fresh water) northward.

[56] 6. On the midshelf of the 62.5°N line, the northward volume transport with an annual mean of 0.62 Sv is year round. The midshelf current is mainly driven by both Pacific-Arctic pressure head and seasonally variable wind forcing. Thus, this current is almost out of phase to the AC in volume and heat transport during winter, i.e., the northward transport in the midshelf versus the southward transport in the Anadyr Current. However, during summer both volume and heat transports are northward for all the three branches; that is, they are in phase because the southwesterly winds are consistent in direction with the Pacific-Arctic pressure head. The salinity transport by AC has a phase difference (or not in phase) with the salinity transports by the midshelf current and ACC. Nevertheless, the salinity transports by the midshelf current and ACC are almost in phase.

[57] Although some rich dynamic and thermodynamic phenomena have been captured and investigated in this study using the Bering-CIOM, the sparse in situ measurements are still the constraint to the model validation. One noticeable shortcoming of the simulations may be that sea ice along the Siberian coast was not reproduced because of the overshooting of the Bering Slope Current, which may transport excessive heat from the east to west coast. Therefore, it is obvious that the ocean circulation along with its heat transport plays an important role in sea ice distribution via both its dynamics and thermodynamics. It is also found that there is a large systematic error in the SSM/I-measured sea ice concentration along the coast due to coastal sea fog, which results in an overestimate of SIC by 10–15%. Thus, caution should be used when interpreting satellite-measured SIC along any coastal seas.

[58] The results shown here should be useful for observationalists to plan their future monitoring designs. Long-term moorings would be very valuable for model validation. Future efforts may be conducted in physical process studies: (1) the coastal and island-induced polynya formation and its impacts on surrounding physical environment, (2) Yukon River plumes under sea ice cover, and (3) upwelling and downwelling variability and dense water formation along the Anadyr Current.

[59] **Acknowledgments.** We thank supports from IARC/JAMSTEC Cooperative Agreement, University of Alaska Costal Marine Institute (CMI) and Minerals Management Service (MMS), and Joint Russian-American Long-term Census of the Arctic (NOAA RUSALCA) International Polar Year modeling project. We want to thank two anonymous reviewers for their very constructive comments, which helped significantly improve this paper. Thanks also go to Cathy Darnell of NOAA GLERL for editing this paper. This is also GLERL contribution 1495.

References

Belkin, I. M., and P. C. Cornillon (2005), Bering Sea thermal fronts from Pathfinder data: Seasonal and interannual variability, *Pac. Oceanogr.*, *3*(1), 6–20.

Blumberg, A. F., and G. L. Mellor (1987), A description of 3-D coastal ocean circulation model, in *Three-Dimensional Coastal Ocean Models*, *Coastal Estuarine Sci.*, vol. 4, edited by N. S. Heaps, pp. 1–16, AGU, Washington, D. C.

Cavalieri, D. J., and S. Martin (1994), The contribution of Alaskan, Siberian, and Canadian coastal polynyas to the cold halocline layer of the Arctic Ocean, *J. Geophys. Res.*, *99*(C9), 18,343–18,362, doi:10.1029/94JC01169.

Clement, J. L., W. Maslowski, L. W. Cooper, J. M. Grebmeier, and W. Walczowski (2005), Ocean circulation and exchanges through the northern Bering Sea—1979–2001, *Deep Sea Res., Part II*, *52*, 3509–3540, doi:10.1016/j.dsr2.2005.09.010.

Coachman, L. K. (1993), On the flow field in the Chirikov Basin, *Cont. Shelf Res.*, *13*, 481–508, doi:10.1016/0278-4343(93)90092-C.

Coachman, L. K., and K. Aagaard (1981), Reevaluation of water transports in the vicinity of Bering Strait, in *The Eastern Bering Sea Shelf: Oceanography and Resources*, vol. 1, edited by D. W. Hood and J. A. Calder, pp. 95–110, Univ. of Wash. Press, Seattle.

Coachman, L. K., and K. Aagaard (1988), Transports through Bering Strait: Annual and interannual variability, *J. Geophys. Res.*, *93*, 15,535–15,539, doi:10.1029/JC093iC12p15535.

Coachman, L. K., and D. A. Handell (1993), ISHTAR, Inner Shelf Transfer and Recycling in the Bering and Chukchi seas, *Cont. Shelf. Res.*, *13*, 473–703.

Coachman, L. K., K. Aagaard, and R. B. Tripp (1975), *Bering Strait: The Regional Physical Oceanography*, 172 pp. pp., Univ. of Wash. Press, Seattle.

Cokelet, E. D., and P. J. Stabeno (1997), Mooring observations of the thermal structure, salinity, and currents in the SE Bering Sea Basin, *J. Geophys. Res.*, *102*, 22,947–22,964, doi:10.1029/97JC00881.

Cokelet, E. D., M. L. Schall, and D. M. Dougherty (1996), ADCP-referenced geostrophic circulation in the Bering Sea Basin, *J. Phys. Oceanogr.*, *26*, 1113–1128, doi:10.1175/1520-0485(1996)026<1113:ARGCIT>2.0.CO;2.

Ezer, T., and G. L. Mellor (1997), Simulations of the Atlantic Ocean with a free surface sigma coordinate ocean model, *J. Geophys. Res.*, *102*(C7), 15,647–15,657, doi:10.1029/97JC00984.

Grebmeier, J. M., and L. W. Cooper (1995), Influence of the St. Lawrence Island polynya upon the Bering Sea benthos, *J. Geophys. Res.*, *100*(C3), 4439–4460, doi:10.1029/94JC02198.

Hermann, A. J., P. J. Stabeno, D. B. Haidvogel, and D. L. Musgrave (2002), A regional tidal/subtidal circulation model of the southeastern Bering Sea: Development, sensitivity analyses and hindcasting, *Deep Sea Res., Part II*, *49*, 5495–5967.

Hibler, W. D., III (1979), A dynamic and thermodynamic sea ice model, *J. Phys. Oceanogr.*, *9*, 815–846, doi:10.1175/1520-0485(1979)009<0815:ADTSIM>2.0.CO;2.

Hibler, W. D., III (1980), Modeling a variable thickness sea ice cover, *Mon. Weather Rev.*, *108*, 1943–1973, doi:10.1175/1520-0493(1980)108<1943:MAVTSI>2.0.CO;2.

Hu, H., Y. Yuan, and Z. Wan (2004), Study on hydrodynamics of Bohai Sea, the Yellow Sea and the East China Sea with wave-current coupled numerical model (in Chinese with an English abstract), *Acta Oceanol. Sin.*, *4*, 19–32.

Hunt, G. L., P. Stabeno, G. Walters, E. Sinclair, R. D. Brodeur, J. M. Napp, and N. A. Bond (2002), Climate change and control of the southeastern Bering Sea pelagic ecosystem, *Deep Sea Res., Part II*, *49*(26), 5821–5853, doi:10.1016/S0967-0645(02)00321-1.

Kinder, T. H., and L. K. Coachman (1978), The front overlaying the continental slope in the eastern Bering Sea, *J. Geophys. Res.*, *83*, 4551–4559, doi:10.1029/JC083iC09p04551.

Kinder, T. H., and J. D. Schumacher (1981), Hydrographic structure over the continental shelf of the southeastern Bering Sea, in *The Eastern Bering Shelf: Oceanography and Resources*, edited by D. W. Hood and J. A. Calder, pp. 31–52, Univ. of Washington Press, Seattle.

Kinder, T. H., J. D. Schumacher, and D. V. Hansen (1980), Observation of a baroclinic eddy: An example of mesoscale variability in the Bering Sea, *J. Phys. Oceanogr.*, *10*, 1228–1245, doi:10.1175/1520-0485(1980)010<1228:OOABEA>2.0.CO;2.

Ladd, C., and N. A. Bond (2002), Evaluation of NCEP/NCAR reanalysis in the NE Pacific and the Bering Sea, *J. Geophys. Res.*, *107*(C10), 3158, doi:10.1029/2001JC001157.

Luchin, V. A., V. A. Menovshchikov, and V. M. Lavrentiev (1999), Thermohaline structure and water masses in Bering Sea, in *Dynamics of the Bering Sea*, edited by T. R. Loughlin and K. Ohtani, pp. 61–91, Univ. of Alaska Sea Grant, Fairbanks, Alaska.

Mantua, N. J., S. R. Hare, Y. Zhang, J. M. Wallace, and R. C. Francis (1997), A Pacific interdecadal climate oscillation with impacts on salmon production, *Bull. Am. Meteorol. Soc.*, *78*, 1069–1078, doi:10.1175/1520-0477(1997)078<1069:APICOW>2.0.CO;2.

Mellor, G. L. (2004), User's guide for a 3-D, primitive equation, numerical ocean model, 56 pp.Atmos. and Oceanic Sci. Program, Princeton Univ., Princeton, N. J.

Mellor, G. L., and L. Kantha (1989), An ice-ocean coupled model, *J. Geophys. Res.*, *94*, 10,937–10,954, doi:10.1029/JC094iC08p10937.

Mellor, G.L., T. Ezer, and L.-Y. Oey (1994), The pressure gradient conundrum of sigma coordinate ocean models, *J. Atmos. Oceanic Technol.*, *11*, 1126–1134, doi:10.1175/1520-0426(1994)011<1126:TPGCOS>2.0.CO;2.

Minobe, S. (1999), Resonance in bidecadal and pentadecadal climate oscillations over the North Pacific: Role in climate regime shifts, *Geophys. Res. Lett.*, *26*(7), 855–858, doi:10.1029/1999GL900119.

Mizobata, K., and S. Saitoh (2004), Variability of Bering Sea eddies and primary productivity along the shelf edge during 1998–2000 using satellite multi-sensor remote sensing, *J. Mar. Syst.*, *50*, 101–111, doi:10.1016/j.jmarsys.2003.09.014.

Mizobata, K., S. Saitoh, S. Shiomoto, T. Miyamura, N. Shiga, M. Toratani, Y. Kajiwara, and K. Sasaoka (2002), Bering Sea cyclonic and anticyclonic eddies observed during summer 2000 and 2001, *Prog. Oceanogr.*, *55*, 65–75, doi:10.1016/S0079-6611(02)00070-8.

Mizobata, K., J. Wang, and S. Saitoh (2006), Eddy-induced cross-slope exchange maintaining summer high productivity of the Bering Sea shelf break, *J. Geophys. Res.*, *111*, C10017, doi:10.1029/2005JC003335.

Mizobata, K., S. Saitoh, and J. Wang (2008), Interannual variability of summer biochemical enhancement in relation to the mesoscale eddy at the shelf break in the vicinity of the Pribilof Islands, Bering Sea, *Deep Sea Res., Part II*, *55*, 1717–1728, doi:10.1016/j.dsr2.2008.03.002.

Niebauer, H. J. (1980), Sea ice and temperature variability in the eastern Bering Sea and relation to atmospheric fluctuations, *J. Geophys. Res.*, *85*, 7507–7515, doi:10.1029/JC085iC12p07507.

Niebauer, H. J., N. A. Bond, L. P. Yakunin, and V. V. Plotnikov (1999), An update on climatology and sea ice of the Bering Sea, in *Dynamics of the Bering Sea*, edited by T. R. Loughlin and K. Ohtani, pp. 29–59, Univ. of Alaska Sea Grant, Fairbanks, Alaska.

Nihoul, J. C. J., P. Adam, P. Brasseur, E. Deleersnijder, S. Djenidi, and J. Haus (1993), Three-dimensional general circulation model of the northern Bering Sea's summer ecohydrodynamics, *Cont. Shelf Res.*, *13*, 509–542, doi:10.1016/0278-4343(93)90093-D.

Office of Coast Survey (2004), Alaska-Aleutian Islands, *NOAA Chart*, 22nd ed., maps 16440, 16460, 16480, 16500, and 16520, Natl. Ocean Serv., NOAA, U.S. Dep. of Commer., Washington, D. C., March.

Ohshima, K. I., and S. Nihashi (2005), A simple ice-ocean coupled model for the Antarctic ice melt season, *J. Phys. Oceanogr.*, *35*, 188–201, doi:10.1175/JPO-2675.1.

Onishi, H., and K. Ohtani (1999), On seasonal and year to year variation in flow of the Alaskan Stream in the central North Pacific, *J. Oceanogr.*, *55*, 597–608, doi:10.1023/A:1007840802296.

Overland, J. E., and P. J. Stabeno (2004), Is the climate of the Bering Sea warming and affecting the ecosystem?, *Eos Trans. AGU*, *85*(33), 309.

Overland, J. E., S. A. Salo, L. H. Kantha, and C. A. Clayson (1999), Thermal stratification and mixing on the Bering Sea shelf, in *Dynamics of the Bering Sea*, edited by T. R. Loughlin and K. Ohtani, pp. 129–146, Univ. of Alaska Sea Grant, Fairbanks, Alaska.

Pease, C. H., S. A. Salo, and J. E. Overland (1983), Drag measurements for first-year sea ice over shallow sea, *J. Geophys. Res.*, *88*(C5), 2853–2862, doi:10.1029/JC088iC05p02853.

Pritchard, R. S., A. C. Mueller, D. J. Hanzlick, and Y.-S. Yang (1990), Forecasting Bering Sea ice edge behavior, *J. Geophys. Res.*, *95*(C1), 775–788, doi:10.1029/JC095iC01p00775.

Roach, A. T., K. Aagaard, C. H. Pease, S. A. Salo, T. Weingartner, V. Pavlov, and M. Kulakov (1995), Direct measurements of transport and water properties through Bering Strait, *J. Geophys. Res.*, *100*(C9), 18,443–18,457, doi:10.1029/95JC01673.

Springer, A. M., and C. P. McRoy (1993), The paradox of pelagic food webs in the northern Bering Sea, III. Patterns of primary production, *Cont. Shelf Res.*, *13*, 575–599, doi:10.1016/0278-4343(93)90095-F.

Springer, A. M., C. P. McRoy, and M. V. Flint (1996), The Bering Sea Green Belt: Shelf-edge processes and ecosystem productivity, *Fish. Oceanogr.*, *5*, 205–223, doi:10.1111/j.1365-2419.1996.tb00118.x.

Stabeno, P. J., and R. K. Reed (1994), Circulation in the Bering Sea Basin observed by satellite-tracked drifters: 1986–1993, *J. Phys. Oceanogr.*, *24*, 848–854, doi:10.1175/1520-0485(1994)024<0848:CITBSB>2.0.CO;2.

Stabeno, P. J., J. D. Schumacher, and K. Ohtani (1999), The physical oceanography of the Bering Sea, in *Dynamics of the Bering Sea*, edited by T. R. Loughlin and K. Ohtani, pp. 1–28, Univ. of Alaska Sea Grant, Fairbanks, Alaska.

Stabeno, P. J., D. G. Kachel, N. B. Kachel, and M. E. Sullivan (2005), Observations from moorings in the Aleutian passes: Temperature, salinity and transport, *Fish. Oceanogr.*, *14*, 39–54, doi:10.1111/j.1365-2419.2005.00362.x.

Steele, M., R. Rebecca, and W. Ermold (2001), PHC: A global ocean hydrography with a high-quality Arctic Ocean, *J. Clim.*, *14*, 2079–2087, doi:10.1175/1520-0442(2001)014<2079:PAGOHW>2.0.CO;2.

Stringer, W. J., J. Zender-Romick, and J. E. Groves (1982), Width and persistence of the Chukchi polynya, 22 pp., Res. Unit 267, Outer Cont. Shelf Environ. Assess. Program, NOAA, Anchorage, Alaska.

Sukhanova, I. N., H. J. Semina, and M. V. Venttsel (1999), Spatial distribution and temporal variability of phytoplankton in the Bering Sea, in *Dynamics of the Bering Sea*, edited by T. R. Loughlin and K. Ohtani, pp. 453–483, Univ. of Alaska Sea Grant, Fairbanks, Alaska.

Tateyama, K., and H. Enomoto (2001), Observation of sea-ice thickness fluctuation in the seasonal ice-covered area during 1992–99 winters, *Ann. Glaciol.*, *33*, 449–456, doi:10.3189/172756401781818707.

Thompson, D. W. J., and J. M. Wallace (1998), The Arctic Oscillation signature in the wintertime geopotential height and temperature fields, *Geophys. Res. Lett.*, *25*, 1297–1300, doi:10.1029/98GL00950.

Thorndike, A. S., D. A. Rothrock, G. A. Maykut, and R. Colony (1975), The thickness distribution of sea ice, *J. Geophys. Res.*, *80*, 4501–4513.

Wallace, J. M., and D. S. Gutzler (1981), Teleconnections in the geopotential height field during the Northern Hemisphere winter, *Mon. Weather Rev.*, *109*, 784–812, doi:10.1175/1520-0493(1981)109<0784:TITGHF>2.0.CO;2.

Walsh, J. J., et al. (1989), Carbon and nitrogen cycling within the Bering/Chukchi seas: Source regions for organic matter effecting AOU demands of the Arctic Ocean, *Prog. Oceanogr.*, *22*, 277–359, doi:10.1016/0079-6611(89)90006-2.

Wang, J., and M. Ikeda (1997), Diagnosing ocean unstable baroclinic waves and meanders using quasi-geostrophic equations and Q-vector method, *J. Phys. Oceanogr.*, *27*, 1158–1172, doi:10.1175/1520-0485(1997)027<1158:DOUBWA>2.0.CO;2.

Wang, J., and M. Ikeda (2000), Arctic Oscillation and Arctic Sea-Ice Oscillation, *Geophys. Res. Lett.*, *27*(9), 1287–1290, doi:10.1029/1999GL002389.

Wang, J., and M. Ikeda (2001), Arctic Sea-Ice Oscillation: Regional and seasonal perspectives, *Ann. Glaciol.*, *33*, 481–492, doi:10.3189/172756401781818626.

Wang, J., and C. N. K. Mooers (1998), Three-dimensional perspectives of the Florida Current: Transport, potential vorticity, and related dynamical properties, *Dyn. Atmos. Oceans*, *27*, 135–149, doi:10.1016/S0377-0265(97)00004-3.

Wang, J., L. A. Mysak, and R. G. Ingram (1994), A numerical simulation of sea-ice cover in Hudson Bay, *J. Phys. Oceanogr.*, *24*(12), 2515–2533, doi:10.1175/1520-0485(1994)024<2515:ANSOSI>2.0.CO;2.

Wang, J., R. Mo, Z. Gao, Z. Yin, and M. Chen (1999), Sensitivity study of coastal plumes, *Acta Oceanol. Sin.*, *18*, 147–166.

Wang, J., M. Jin, V. Patrick, J. Allen, D. Eslinger, C. N. Mooers, and T. Cooney (2001), Numerical simulation of the seasonal ocean circulation patterns and thermohaline structure of Prince William Sound, Alaska, *Fish. Oceanogr.*, *10*, 132–148, doi:10.1046/j.1054-6006.2001.00035.x.

Wang, J., Q. Liu, and M. Jin (2002), A user's guide for a coupled ice-ocean model (CIOM) in the pan-Arctic and North Atlantic oceans, *Tech. Rep. 02-01*, 65 pp., Int. Arct. Res. Cent., Fairbanks, Alaska.

Wang, J., et al. (2003a), Working towards improved small-scale sea ice and ocean modeling in the Arctic seas, *Eos Trans. AGU*, *84*(34), 325.

Wang, J., M. Ikeda, and F. Saucier (2003b), A theoretical, two-layer, reduced-gravity model for descending dense water flow on continental slopes, *J. Geophys. Res.*, *108*(C5), 3161, doi:10.1029/2000JC000517.

Wang, J., B. Wu, C. Tang, J. E. Walsh, and M. Ikeda (2004a), Seesaw structure of subsurface temperature anomalies between the Barents Sea and the Labrador Sea, *Geophys. Res. Lett.*, *31*, L19301, doi:10.1029/2004GL019981.

Wang, J., M. Jin, D. Musgrave, and M. Ikeda (2004b), A numerical hydrological digital elevation model for freshwater discharge into the Gulf of Alaska, *J. Geophys. Res.*, *109*, C07009, doi:10.1029/2002JC001430.

Wang, J., Q. Liu, M. Jin, M. Ikeda, and F. J. Saucier (2005a), A coupled ice-ocean model in the pan-Arctic and the northern North Atlantic Ocean: Simulation of seasonal cycles, *J. Oceanogr.*, *61*, 213–233, doi:10.1007/s10872-005-0033-3.

Wang, J., M. Ikeda, S. Zhang, and R. Gerdes (2005b), Linking the northern hemisphere sea ice reduction trend and the quasi-decadal Arctic Sea Ice Oscillation, *Clim. Dyn.*, *24*, 115–130, doi:10.1007/s00382-004-0454-5.

Watanabe, E., J. Wang, T. Sumi, and H. Hasumi (2006), Arctic Dipole and its contribution to sea ice exports in the 20th century, *Geophys. Res. Lett.*, *33*, L23703, doi:10.1029/2006GL028112.

Woodgate, R. A., and K. Aagaard (2005), Revising the Bering Strait freshwater flux into the Arctic Ocean, *Geophys. Res. Lett.*, *32*, L02602, doi:10.1029/2004GL021747.

Woodgate, R., T. J. Weingartner, and K. Aagaard (2005), A year in the physical oceanography of the Chukchi Sea: Moored measurements from autumn 1990–1991, *Deep Sea Res., Part II*, *52*, 3116–3149, doi:10.1016/j.dsr2.2005.10.016.

Wu, B., J. Wang, and R. Zhang (2004), Effects of intraseasonal variations of the Arctic Oscillation on the Barents Sea, *Polar Meteorol. Glaciol.*, *18*, 82–95.

Yao, T., C. L. Tang, and I. K. Peterson (2000), Modeling the seasonal variation of sea ice in the Labrador Sea with a coupled multicategory ice model and the Princeton ocean model, *J. Geophys. Res.*, *105*, 1153–1165, doi:10.1029/1999JC900264.

H. Hu, Cooperative Institute for Limnology and Ecosystems Research, School of Natural Resources and Environment, University of Michigan, 4840 S. State Road, Ann Arbor, MI 48108, USA. (hghu@umich.edu)

K. Mizobata, Department of Ocean Sciences, Tokyo University of Marine Science and Technology, 4-5-7, Kounan, Minato-ku, Tokyo 108-8477, Japan. (mizobata@kaiyodai.ac.jp)

S. Saitoh, Graduate School of Fisheries Sciences, Hokkaido University, Hakodate, Hokkaido 041-8611, Japan. (ssaitoh@salmon.fish.hokudai.ac.jp)

J. Wang, Great Lakes Environmental Research Laboratory, NOAA, 4840 S. State Road, Ann Arbor, MI 48108, USA. (jia.wang@noaa.gov)